

9-15-2020

Large Scale Upper-Level Precursors for Dust Storm Formation Over North Africa and Poleward Transport to the Iberian Peninsula. Part I: An Observational Analysis

J.A. G. Orza

Universidad Miguel Hernández de Elche, ja.garcia@umh.es

Michael L. Kaplan

Embry-Riddle Aeronautical University, Michael.Kaplan@erau.edu

S. Dhital

Desert Research Institute

S. Fiedler

University of Cologne

Follow this and additional works at: <https://commons.erau.edu/publication>



Part of the [Atmospheric Sciences Commons](#), and the [Meteorology Commons](#)

Scholarly Commons Citation

Orza, J. G., Kaplan, M. L., Dhital, S., & Fiedler, S. (2020). Large Scale Upper-Level Precursors for Dust Storm Formation Over North Africa and Poleward Transport to the Iberian Peninsula. Part I: An Observational Analysis. *Atmospheric Environment*, 237(15). <https://doi.org/10.1016/j.atmosenv.2020.117688>

This Article is brought to you for free and open access by Scholarly Commons. It has been accepted for inclusion in Publications by an authorized administrator of Scholarly Commons. For more information, please contact commons@erau.edu.

1 **Large Scale Upper-level Precursors for Haboob and Mountain Wave Dust Storm**
2 **Formation over North Africa and Poleward Transport of Dust to the Iberian**
3 **Peninsula. Part I: An Observational Analysis**
4

5 **J. A. G. Orza^a, S. Dhital^b, and M. L. Kaplan^c**

6 ^aSCOLAb, Department of Applied Physics, Universidad Miguel Hernández de Elche, Av. de la
7 Universidad s/n, 03202 Elche, Spain. ja.garcia@umh.es

8 ^bDivision of Atmospheric Sciences, Desert Research Institute, 2215 Raggio Parkway, Reno, NV
9 89512, USA. sarojdhital11@gmail.com

10 ^cApplied Meteorology Program, Embry-Riddle Aeronautical University, 3700 Willow Creek
11 Road, Prescott, AZ 86301, USA. kaplanm1@erau.edu

12
13
14
15 Corresponding author: J. A. G. Orza (ja.garcia@umh.es)

16 Jose A. Garcia Orza

17 SCOLAb, Department of Applied Physics

18 Universidad Miguel Hernandez de Elche

19 Av. de la Universidad, s/n

20 03202 Elche (Spain)

21 Tel. + 34 966658580

22

23 **Highlights**

24

- 25 • Three Saharan dust events with strong impact poleward over the Iberian Peninsula
- 26 • A common upper-level precursor for events with substantial subsynoptic differences
- 27 • Two polar stream Rossby wave breaks instrumental for dust ablation and transport
- 28 • A sequence of multi-scale adjustments organizes the Saharan dust storms

29

30 Abstract

31 The analysis of three extreme African dust outbreaks over the Iberian Peninsula (IP) shows that a
32 double Rossby wave breaking (RWB) process in the polar jet (PJ) creates the conditions for dust
33 storm formation over subtropical deserts in North Africa and the restructuring of upper-level air
34 flows critical for the dust transport poleward after ablation. Two consecutive anticyclonic RWBs
35 initiate over the IP and the adjacent Atlantic, the first commencing 10 days before dust reaches
36 the IP and the second three to five days later. The first RWB becomes quasi-stationary over the
37 eastern Mediterranean when the second RWB develops. In turn, the first RWB blocks
38 downstream propagation of the second, which is amplified by energy reflection poleward from
39 the first break causing vortex intensification and equatorward propagation over the Atlas as well
40 as a strengthening and coupling of the subtropical jet (STJ) to circulations in the ITCZ. Zonal
41 flows are blocked and sustained low-level northeasterlies/easterlies are induced across northwest
42 Africa. The three events present substantial differences in the location and geometry of key
43 upper- and low-level subsynoptic features that organize the dust storms over the Sahara
44 following the second break. Dust lifted by either the cold outflow from convective downdrafts or
45 by orographic gravity waves interacts with terrain-induced and larger scale circulations and is
46 transported to the IP. The location of the cyclonic large scale signal from the second RWB to the
47 west or over the Atlas and the blocking of zonal flows are key for the poleward dust transport.

48 **Keywords:** Saharan dust storm, upper-level disturbance, Rossby wave breaking, multi-scale
49 adjustment, poleward dust transport.

50 1 Introduction

51 Mineral dust mobilized in dry areas of North Africa impacts the local environment and
52 also distant downwind areas. North African dust emissions are advected primarily to the tropical
53 North Atlantic within the Saharan Air Layer (e.g. Prospero, 1999; Adams et al., 2012; Gläser et
54 al., 2015). Yet, a significant fraction is transported northwards across the Mediterranean (e.g.,
55 Moulin et al., 1998; Gkikas et al., 2009; Israelevich et al., 2012; Querol et al., 2009; Pey et al.,
56 2013; Varga et al., 2014; Marinou et al., 2017). Northeasterly/easterly low-level trade winds over
57 northern Africa, commonly referred to as Harmattan winds, prevail in the area and therefore
58 normal conditions do not favor the poleward advection to the Mediterranean and Europe. The
59 intensity of these winds can be modulated by cold air outbreaks in Western Europe resulting in
60 stronger dust transport over the Tropical North Atlantic (e.g., Fiedler et al., 2015; Schepanski et
61 al., 2017). As a consequence, intense dust export has a highly episodic nature.

62 Much effort has been made in the last decades to characterize the impact over Europe of
63 the African dust outbreaks in terms of aerosol concentrations, composition, and ground-level,
64 column-integrated and vertically-resolved optical properties. That work has resulted in a better
65 knowledge of the spatial extent and variability of that impact, on time scales spanning from
66 diurnal to inter-annual. Similarly, the description of the synoptic scenarios and major pathways
67 leading to dust transport towards Europe has been addressed to a great extent. However, the
68 detailed analysis of the multi-scale atmospheric dynamical processes and features leading to the
69 mobilization of dust in northern Africa and its subsequent transport polewards has not received
70 the same attention.

71 PM_{10} dust concentrations from background air quality monitoring stations and vertically-
72 integrated dust measurements from satellite and sun photometers in the Mediterranean show that

73 both the dust burden and the frequency of dust episodes decrease poleward, as distance increases
74 from the sources (Querol et al., 2009; Pey et al., 2013; Gkikas, 2013). Longitudinal differences
75 are also found, with more dust in spring over the eastern Mediterranean and more dust in
76 summertime over the western part (Moulin, 1998; Gkikas et al., 2009; Israelevich et al., 2012;
77 Querol et al., 2009). Higher PM₁₀ concentrations are found in the eastern basin, in part due to the
78 additional contribution of Middle East sources that increase the dust load and also because
79 during summer the dust reaches the western Mediterranean with a great vertical extent and
80 therefore surface concentrations are comparatively lower than the columnar ones (Gkikas et al.,
81 2013; Pey et al., 2013). Dust is the largest contributor to PM₁₀ in the regional background sites of
82 Spain (up to 45%), Greece and Cyprus (35%), according to Pey et al. (2013).

83 The synoptic patterns of poleward transport of dust to the Mediterranean are different in
84 the western and eastern basins (see Varga et al., 2014, for a comprehensive picture of the mean
85 synoptic situations). In the western Mediterranean dust events are dominant in summer and
86 sporadic in spring. Dust is typically transported by southwesterly flows associated with: 1) the
87 intensification and migration northwards of the North African High, located above 850 hPa,
88 which transports uplifted dust in its western flank and/or 2) a trough of low pressure extending
89 southwards to northwestern Africa (Rodríguez et al., 2001; Escudero et al., 2005; Salvador et al.,
90 2014; see also Cuevas et al., 2017). In the eastern Mediterranean, dust transport is basically
91 linked to cyclonic activity (Ganor et al., 2010; Dayan et al., 2008; Flaounas et al., 2015), in the
92 form of mid-latitude Mediterranean cyclones and depressions formed in the lee of the Atlas
93 (commonly termed Sharav cyclones). These depressions are displaced east or northeastward
94 along the Mediterranean mostly in spring and winter, carrying dust in the warm sector ahead the
95 cyclone. In the central Mediterranean, summer dust episodes are similar to those of the western
96 part with the governing centers of action located further to the east; in spring, the North African
97 High located over Libya may block the eastward migration of the cyclones and then dust impact
98 is restricted to the central Mediterranean (see Moulin et al., 1998; Israelevich et al., 2002; Barkan
99 et al., 2005).

100 Moreover, a considerable effort has been made in recent years to identify the dust source
101 areas and the main processes leading to dust entrainment in North Africa (e.g., Knippertz &
102 Todd, 2012, and references therein; Schepanski et al., 2007, 2009; Fiedler et al., 2014, 2015;
103 Pokharel et al., 2017). Over the drylands of North Africa, dust is mainly mobilized in deflatable
104 areas by low-level jets, synoptic scale circulations, convective features and downslope winds. In
105 particular the penetration of upper-level troughs into low latitudes represents a large scale
106 forcing on the low-level dynamics associated with intense dust emission episodes over North
107 Africa (e.g., Alpert & Ziv, 1989; Reiff et al., 1986; Barkan et al., 2005; Emmel et al., 2010;
108 Fiedler et al., 2014). Trough amplification and thinning accompanying the equatorward breaking
109 of Rossby waves (RWB) has been observed to trigger heavy precipitation events as well as
110 massive dust mobilization over North Africa (e.g., Thorncroft & Flocas, 1997; Knippertz & Fink,
111 2006; Fiedler et al., 2015; Wiegand & Knippertz, 2014; Saroj et al., 2020) and the Middle East
112 (e.g., de Vries et al., 2017). The advection of PV-rich and cold air promotes dynamical ascent
113 and a reduction of the static stability that destabilizes the atmosphere. In low-level baroclinic
114 areas it can initiate cyclogenesis (e.g., Thorncroft & Hoskins, 1990; Thorncroft & Flocas, 1997).
115 RWB climatologies show the summer predominance for RWB although breaking waves
116 penetrate far into the subtropics mainly in winter and spring. It is consistently shown that the
117 downstream end of the North Atlantic storm track is a preferred region of RWB (Thorncroft et

118 al., 1993; Postel & Hitchman, 1999; Abatzoglou & Magnusdottir, 2006; Wernli & Sprenger,
119 2007; Wiegand & Knippertz, 2014).

120 Although extratropical upper-level disturbances displaced equatorward are found in most
121 major African dust outbreaks in Europe, only a few studies have analyzed in detail the dynamical
122 processes involved in the deflation and the subsequent poleward transport of dust, e.g.,
123 Thorncroft & Flocas (1997). Quite recently, Francis et al., (2018) have described an episode of
124 African dust transported to Greenland in which both dust ablation and transport polewards are
125 forced by the Polar Jet.

126 Three case studies are analyzed in this paper. It is shown that a double Rossby wave
127 break process is the common upper-level large-scale precursor that organizes a favorable
128 environment for dust ablation and poleward transport. The three episodes were driven by
129 anticyclonic Rossby wave breaking (RWB) in the polar troposphere with strong baroclinic
130 forcing of moist convection, which was critical for dust ablation. The cyclonic large scale signal,
131 resulting from positive-tilting and baroclinic trough thinning associated with the double RWB
132 process, triggered convection and was also responsible for dust transport to the Iberian Peninsula
133 (IP). The episodes represent a substantial perturbation of the mean synoptic situation and the
134 strength of both the large scale extratropical cold air intrusion and the organized convection at
135 finer scales is not unrelated to the transitional periods (late summer/early autumn and late
136 winter/early spring) in which they occurred. The cases are also unusual in terms of their impact
137 over the IP. The low-level processes, moisture sources and circulations were distinct in each
138 episode, though they had common large scale precursors at upper-levels.

139 This paper, Part I, describes the synoptic and larger subsynoptic-scale processes leading
140 to the development of a favorable environment for moist convection or mountain wave
141 formation, dust ablation, and transport to the Iberian Peninsula, while in Part II dust mobilization
142 and transport is described in detail at the finer mesoscales of motion with a high-resolution
143 numerical model and a large number of surface observations.

144 **2 Data and Methods**

145 Data from the European Centre for Medium-Range Weather Forecasts (ECMWF) Interim
146 reanalysis (ERA-Interim; Dee et al., 2011) is used to study the three cases. Data is available at
147 00, 06, 12 and 18 UTC with 0.75 deg horizontal resolution. Potential vorticity (PV), wind speed
148 and the Montgomery stream function (TSI) on the 330 K isentropic surface are used to analyze
149 the upper-level dynamics and identify RWBs. Higher isentropes are usually preferable for
150 identifying dynamical processes around the subtropical tropopause but the 330 K surface better
151 captures RWBs in the polar stream particularly in such cold events over the North Atlantic and
152 northwestern Europe. Sea level pressure, 2 m air temperature as well as wind speed, potential
153 temperature, and geopotential height at 925 hPa allow the analysis of the near-surface
154 environment. Low-level humidity and convective available potential energy (CAPE) is
155 calculated to support convection initiation. Vertical cross-sections of PV, potential temperature,
156 u-w and v-w wind components, and radiosonde upper-air observations are also analyzed for the
157 interpretation of the case studies.

158 False-color RGB Dust imagery from the Spinning Enhanced Visual and Infrared Imager
159 (SEVIRI) onboard the geostationary Meteosat Second Generation satellites (MSG), available for
160 both daytime and nighttime with 15 min temporal resolution and a resolution of 3 km at the sub-

161 satellite point, is applied to follow the formation and evolution of the dust plumes when not
162 covered by clouds. This imagery also provides information on convective cloud development
163 and low-level moisture that can be associated with moist convection and cold pools as well as
164 haboob formation. RGB dust composites make use of three thermal channels to contrast the
165 brightness temperature signal among surface, cloud, and dust (Lensky and Rosenfeld, 2008) in a
166 color scheme in which dust appears magenta. A number of limitations of the product, including
167 some dependence on column water vapor, lower tropospheric lapse rate, and the altitude of lifted
168 dust, have been identified (see Brindley et al., 2012 and references therein), though this dataset
169 has already proven to be highly useful in most cases. MSG dust imagery supports the description
170 of the smaller scale processes in this paper.

171 **3 Three case studies**

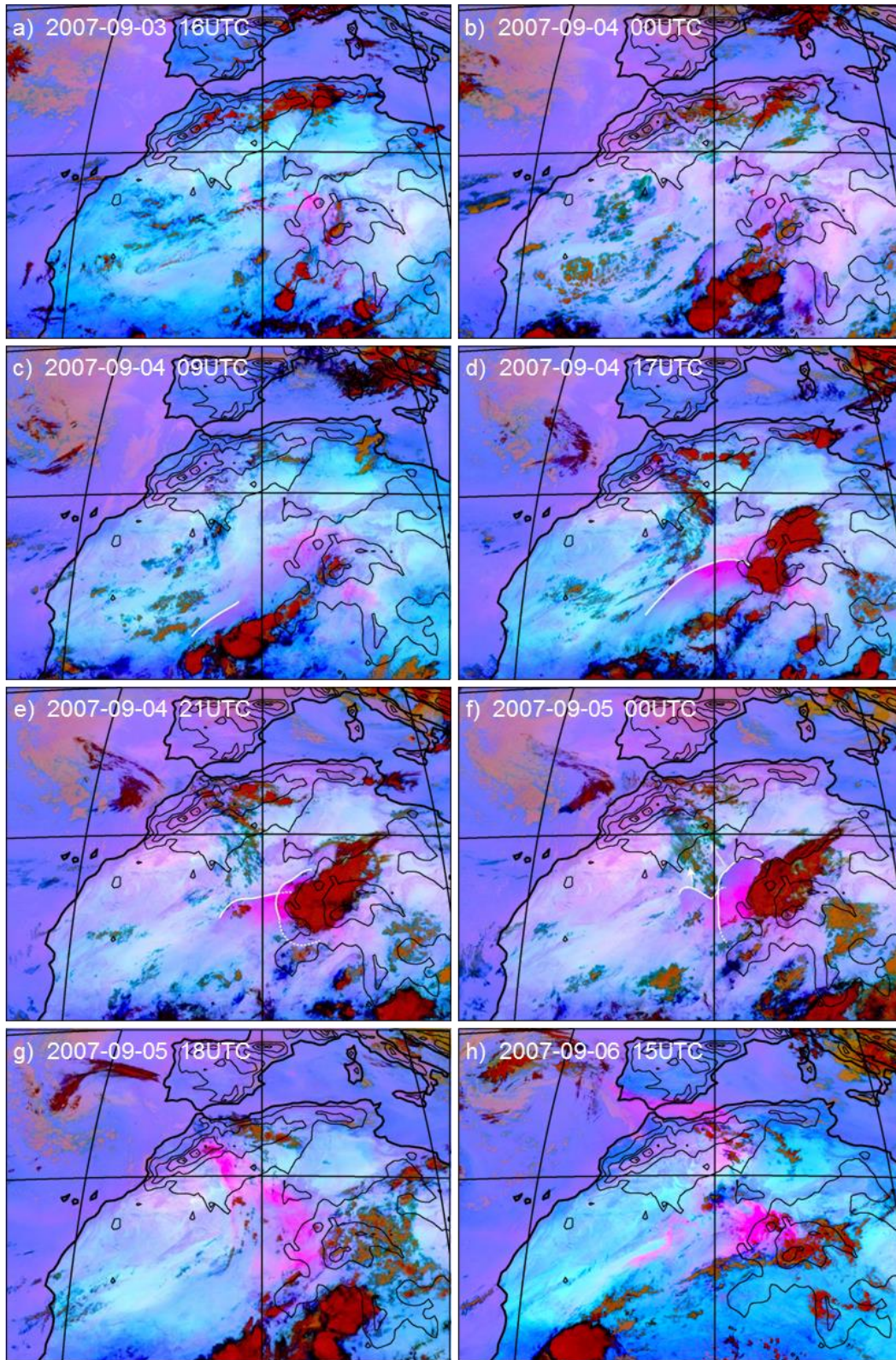
172 All three episodes, i.e., September 2007 (S07), October 2008 (O08) and February 2016
173 (F16) have already been studied with a focus on their strong impact over the IP by a number of
174 authors. While the October 2008 episode represents a case of extreme impact at the ground level,
175 the September 2007 case is an example of dense dust layers reaching the southern IP at mid-
176 levels in the troposphere, and on February 2016 both middle levels and then the ground were
177 strongly impacted across the IP. MSG dust imagery (Figures 1-3) shows the dust plumes
178 emanating from different source areas over North Africa in each case study and their propagation
179 poleward to the IP.

180 Very high records of aerosol optical depth (AOD) accompanied by very low Ångström
181 exponent (AE) values were registered on September 6 at Granada during the September 2007
182 case (Guerrero-Rascado et al., 2009), consistent with the MSG dust imagery in Figure 1h. Only
183 one other episode (on February 2017) has shown substantially higher AODs in southern Spain
184 than this case study. PM₁₀ levels were, however, moderate in agreement with the lidar profiles
185 for this event, which identified a thick dust layer at 3-4 km asl over Granada (Guerrero-Rascado
186 et al., 2009). The AOD was also high with low AE at other AERONET stations in southwestern
187 Spain and Portugal during the event (Antón et al., 2012). Figures 1c-1f shows a haboob
188 emanating from a line of convective cells to the southwest of Adrar des Iforas by September 4
189 that spreads to the northeast and eventually merges with a second haboob generated when
190 convection is triggered in the western slope of the Hoggar. The merger propagates to the
191 northwest and reaches the IP in the early morning of September 9, Figures 1g-1h.

192 The October 2008 case was the strongest one in terms of PM₁₀ concentrations ever
193 registered in a regional background station in southern Spain (Cabello et al., 2012). During the
194 event, up to 89% of the air quality monitoring stations in the country surpassed the 50 µg m⁻³ EU
195 daily limit value for PM₁₀, with the highest daily mean PM₁₀ concentration of 378 µg m⁻³ found
196 at Malaga on October 11. Zonal winds after October 13 swept the dust plume to western and
197 central Europe, as registered in subsequent days over several countries (see references in Cabello
198 et al., 2012). A haboob starts to become visible on the MSG dust imagery at 13 UTC on
199 September 9, propagating southwestwards from below the convective clouds formed to the south
200 of the Moroccan Atlas (Figure 2d shows the image one hour later). From the early morning of
201 October 10 the dust plume turns cyclonically polewards and reaches southern Spain in the
202 morning of October 11, Figures 2f-2h.

203 During the February 2016 case, two distinct dust plumes reached the IP one after the
204 other. Both the Iberian Ceilometer Network (Cazorla et al., 2017) and the lidars operating in

205 southeastern and northeastern Spain (Titos et al., 2017) showed elevated plumes at heights below
206 4000 m at the time of the dust arrival, which subsequently settled down and entrained into the
207 boundary layer. During this episode, 90% of the air quality stations in Spain exceeded the EU
208 daily limit value (Titos et al., 2017). Radiative forcing at the top of the atmosphere in this event
209 was not significantly larger than in other dust episodes (Sorribas et al., 2017) but the intensity
210 was unseasonably strong. The first dust plume starts to be noticeable, Figure 3b, in the foothills
211 of the Saharan Atlas in the MSG dust imagery by 10 UTC, February 20. The plume is elevated
212 and then propagates northwestwards, reaching the IP at 18 UTC (Figure 3e), and is deformed
213 cyclonically over it in the following hours. The second dust plume (Figure 3h) impacted
214 subsequently the eastern IP. It is associated with the outflow from deep convection within the
215 moist tropical plume extending northeastward over North Africa towards the western
216 Mediterranean.
217



218

219 **Figure 1.** Sequence of MSG-SEVIRI dust RGB images to illustrate the development of
 220 convective clouds and haboob formation in the September 2007 case. White lines indicate
 221 relevant dust fronts. Terrain contours at 500 m intervals.

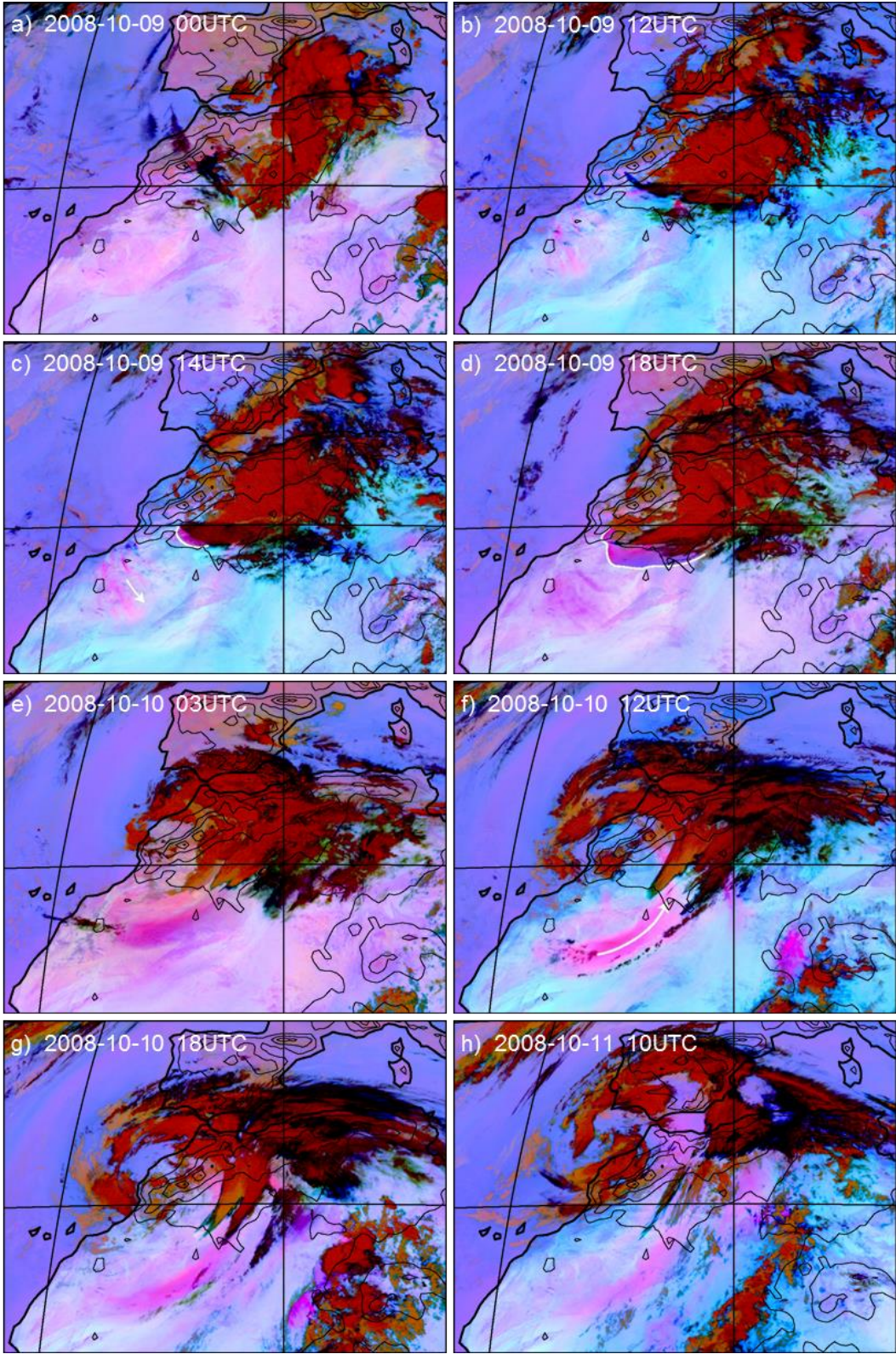
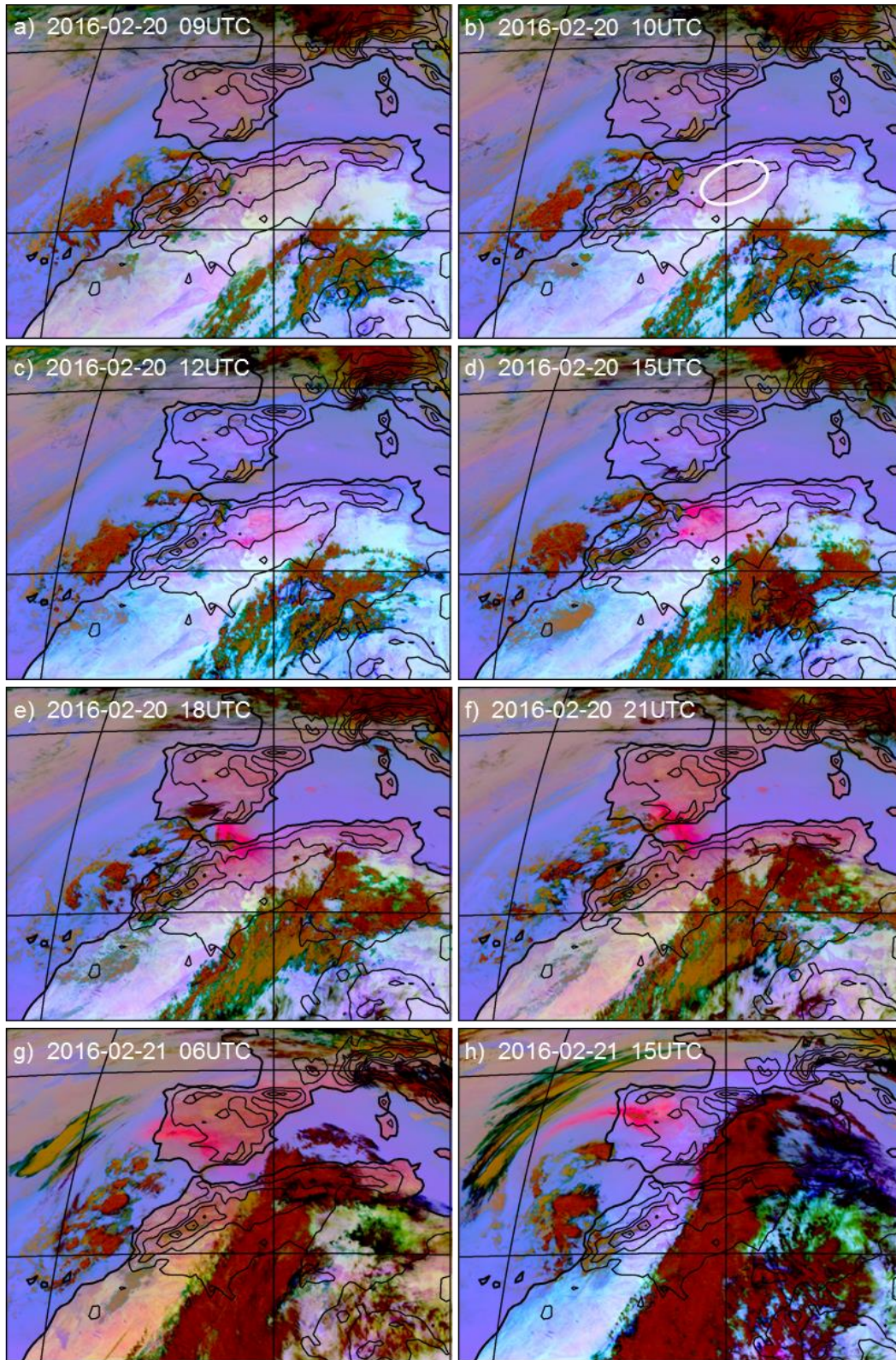


Figure 2. As in Figure 1 but for the October 2008 case.

222
 223
 224
 225



226
 227
 228
 229

Figure 3. As in Figure 1 but for the February 2016 case. The white oval indicates where and when dust mobilization starts to become visible.

230 **4 Synoptic Scale Environment for Haboob Genesis**

231 4.1 Synoptic Precursor Circulations: Double RWBs

232 It is important to understand the synoptic precursors that first develop almost ten days
233 prior to the arrival of dust in the Iberian Peninsula. They trigger low-level jet formation
234 processes that lead to dust ablation for all three case studies during which multiple low-level jets
235 develop, most notably but not exclusively: 1) one from the east extending along the
236 Mediterranean coasts of Algeria, Tunisia, and Libya and 2) one from southwestern Algeria that
237 rises up over the Atlas.

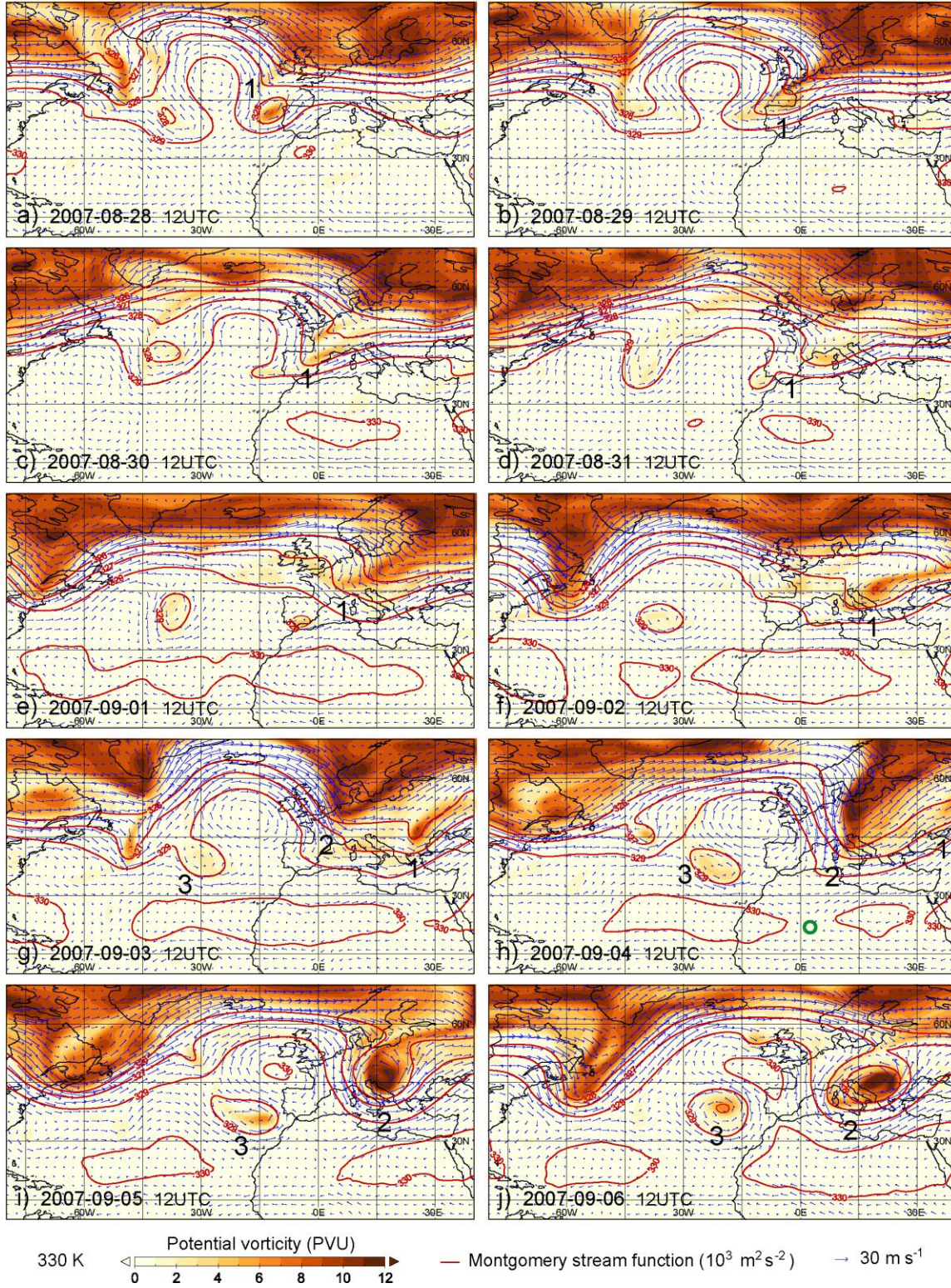
238 The specific synoptic precursors to low-level jets, haboobs, and dust transport in all three
239 cases are remarkably similar in structure and location and all three involve a double RWB in the
240 polar jet stream (PJ) offshore of and over most of Europe. The locations of the RWB do vary
241 longitudinally among the three case studies but what makes them similar and favorable for dust
242 transport poleward to southwestern Europe is how far west in Europe and North Africa they
243 affect. As noted by Postel and Hitchman (1999) and Abatzoglou and Magnusdottir (2006), RWB
244 is accompanied and determined by the unique restructuring of the tropopause, typically depicted
245 on the 350K isentropic surface, in which wave amplification and rotation creates a meridional
246 isentropic potential vorticity (IPV) reversal as well as substantial zonal gradients in IPV. Zonal
247 momentum is converted into eddy momentum by baroclinic and/or barotropic processes. The
248 meridional reversal zone or “surf zone” is often depicted on the 350K isentropic surface and also,
249 more often than not, associated with the subtropical jet stream (STJ). In these three dust storm
250 case studies the evidence points to RWB occurring on the polar tropopause as very cold air is
251 involved in the breaking process consistent with the lower tropopause in the proximity of the
252 polar jet. Because this air involved in the RWBs is so cold in the three case studies, we will focus
253 on IPV on the 330K surface that roughly couples the region in between both upper-level jets in
254 spite of its lack of widespread use in the literature.

255 Two wave breaks occur, the first commencing roughly ten days prior to dust storm
256 formation in a rather similar manner in all three case studies. Figures 4-6 depict, for all three
257 cases, 330K IPV, wind vectors, and Montgomery stream function (TSI) for the 24-hourly periods
258 for all ten-day 1200 UTC (0000 UTC for F16) analyses including the period five-ten days prior
259 to the arrival of dust over the IP. The meridional IPV reversal on the 330K surface allows
260 identifying the RWBs in these figures and labels indicate their location in each case: “1” is used
261 for the first RWB and “2” for the second RWB, while “3” points in the S07 case to a
262 strengthened PV vortex. While RWB can be cyclonic, in all three case studies both breaks are
263 anticyclonic. The anticyclonic sheared waves break in equatorward direction, consistent with
264 trough thinning equatorward and upstream (i.e., the troughs are oriented in a NE-SW direction)
265 accompanying IPV reversal, as observed in Figures 4-6. As noted in section 2, above, all fields in
266 this paper, Part I, are derived from ECMWF reanalyses and remotely-sensed observations.
267 According to the satellite observations (Figures 1-3), the dust arrives in multiple plumes which
268 follow just 1-3 days after the second wave breaking period. As will be shown in a companion
269 paper, Part II, based on numerical simulations, the plumes of dust are ablated by low-level
270 outflow from massive convection and subsequent haboobs in the S07 and O08 cases, whose
271 organization is tied to circulations established by the two wave breaks. In the F16 case, the
272 combined effects of these circulations and the orographic gravity wave activity force upslope
273 low-level flow over the Saharan Atlas, dust deflation and rising motion. Ultimately these two

274 wave breaking events are instrumental in setting up the low-level mass perturbations and jets
275 that, in turn, organize complex subsynoptic features, i.e., haboobs and confluence zones
276 responsible for dust ablation and its transport poleward.

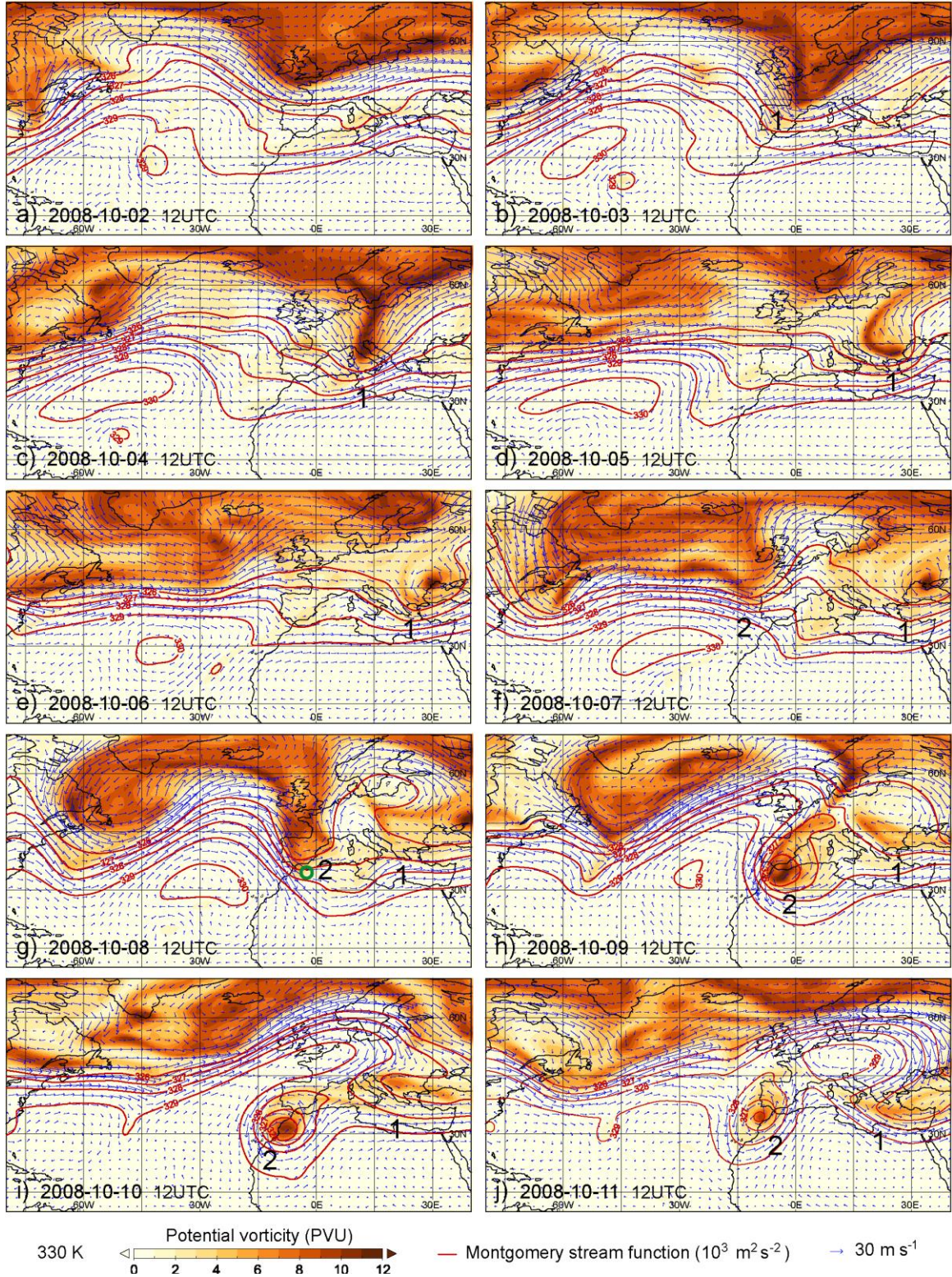
277 As noted in Abatzoglou and Magnusdottir (2006), RWB is facilitated when the PJ and
278 STJ are unambiguously split and not continuously linked. Ample proof can be seen depicting this
279 separation of the PJ and STJ ten days before dust arrives over the Iberian Peninsula in Figures 4-
280 6. In all three cases the PJ and STJ are well-developed but separated by a substantial meridional
281 distance along the North African and European Coasts with S07 being quite interesting because
282 the STJ actually resembles a tropical plume structure. This plume is emanating from a tropical
283 disturbance over the North Atlantic consistent with the late summer time period of this event
284 between 30 and 45N. The separation between the two streams is quite evident at the beginning of
285 each period in Supporting Information Figure S1 which represents a precursor period to the first
286 break. In S07, on 26 August the STJ is located primarily between 30 and 45N latitude while the
287 PJ is very close to 60N. In O08 the STJ is equatorward of 30N and PJ roughly at 55N on October
288 1. In F16 the STJ is between 15 and 30N while the PJ is closer to 45N on February 10. The
289 subsequent RWBs are initiated in the polar stream with very substantial poleward gradients in
290 the Montgomery stream function values on isentropic surfaces indicating very cold air poleward
291 of the PJ (Figures 4-6).

292 The RWB #1 event occurs from August 28 to August 30 in S07 over the northeastern
293 Atlantic with a substantial strengthening of the IPV gradient over France and northwestern
294 Spain. In O08 the first break occurs from the October 2-4 period reversing the IPV over southern
295 Spain and upstream over the adjacent Atlantic equatorward to coastal North Africa. This is
296 clearly 15-30 degrees west of the S07 break which affects the interior part of western Europe
297 while the O08 is primarily offshore. The F16 break is more closely aligned with the O08 case
298 study thus strengthening the meridional gradient of IPV southwest of Spain over the Atlantic and
299 also over North-west Africa (February 14-16). Accompanying RWB #1, by about seven-eight
300 days before the dust storms, the IPV reversal over western Europe and the eastern Atlantic is
301 complete and the positively-tilted troughs which have formed and the cold air, indicated by low
302 poleward TSI values, transported equatorward into the northern Mediterranean with S07,
303 southern Mediterranean with O08, and northern Africa with F16 in Figures 4-6, respectively.
304 This transport has caused the wind to adjust to the mass resulting in an equatorward and
305 downstream intensification of the STJ in all cases. The STJ was initially maintained as the
306 momentum maxima surrounding the Hadley cell which was well-fortified by very hot air
307 poleward of the Sahara over North Africa or in the case of S07 by an offshore tropical
308 disturbance.



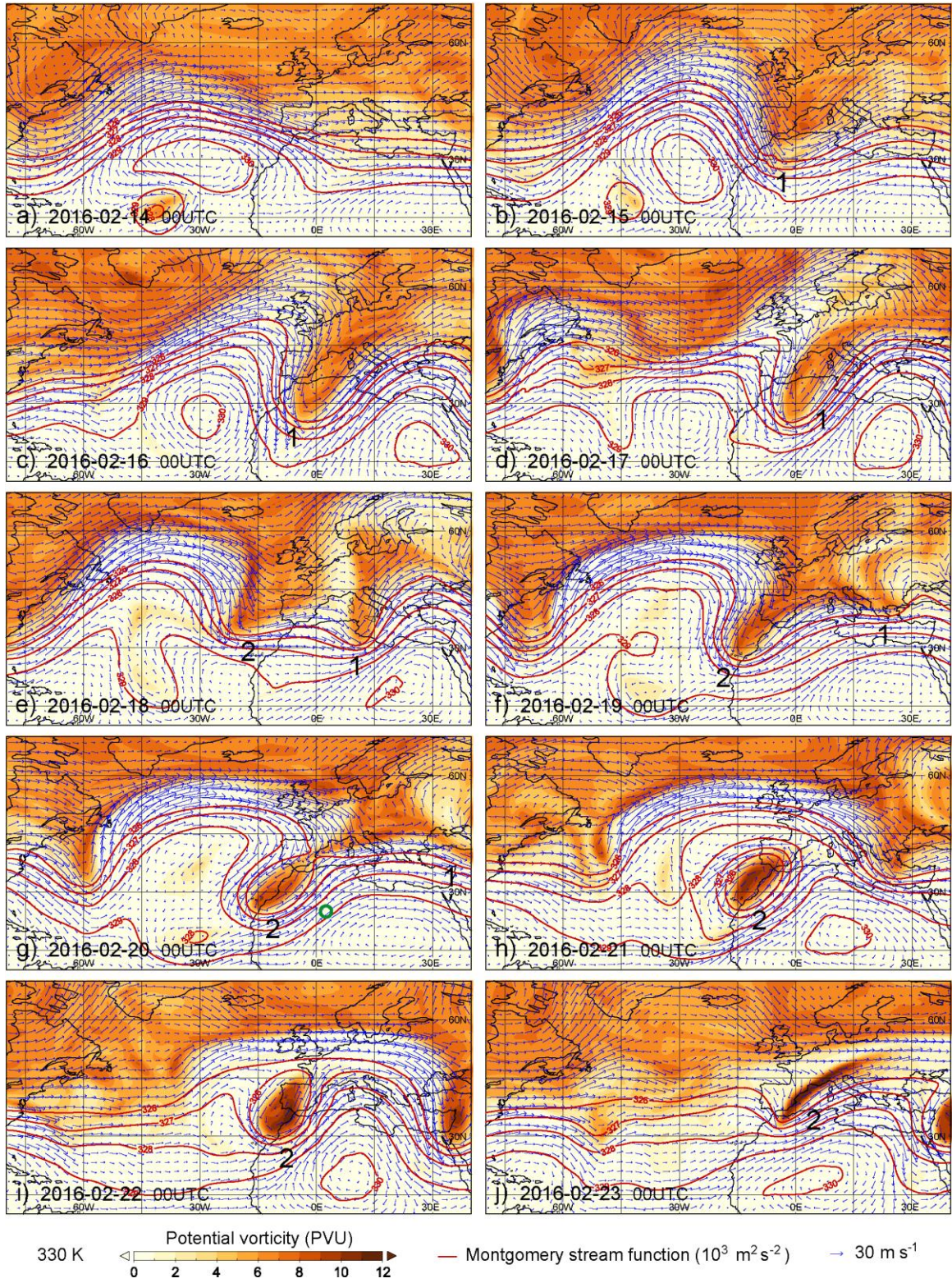
309

310 **Figure 4.** Potential vorticity (shaded), wind vectors and Montgomery stream function (red
 311 contours) at the 330K surface for the ten days preceding the arrival of dust to the IP on the
 312 September 2007 case. The green circle in the plot of September 4 indicates the same position as
 313 in the vertical cross section of Figure 10a.



314

315 **Figure 5.** As in Figure 4 but for the October 2008 case. The green circle in the plot of October 8
 316 indicates the same position as in the vertical cross section of Figure 10b.



317

318

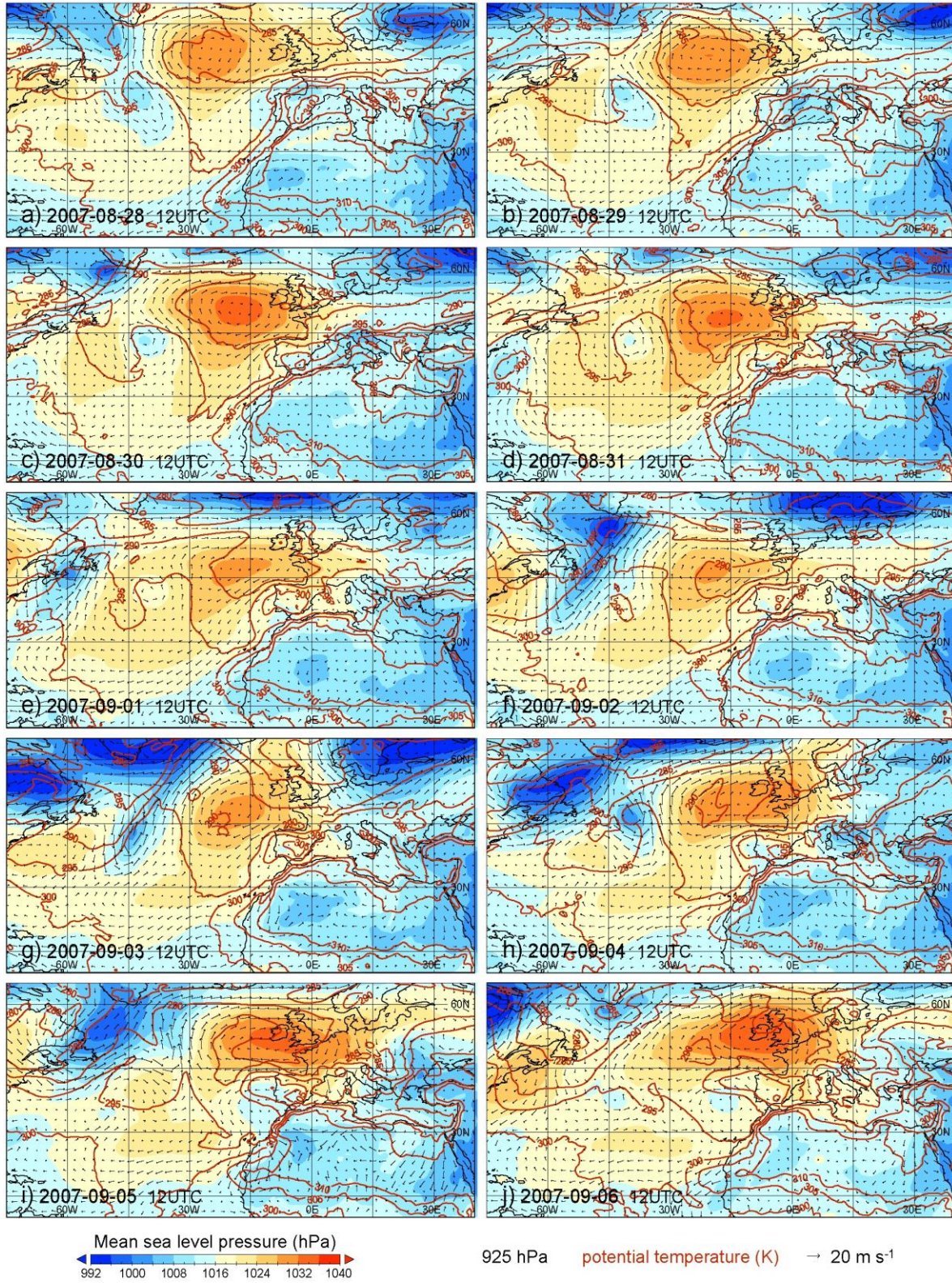
319

Figure 6. As in Figure 4 but for the February 2016 case. The green circle in the plot of February 20 indicates the same position as in the vertical cross section of Figure 10c.

320 To diagnose the low-level effects of these RWBs, which can be seen in Figures 7-9 at the
321 same time intervals as for Figures 4-6, are depicted the mean sea level pressure, 925 hPa
322 potential temperature, and 925 hPa wind vectors. In these figures the first breaking process has
323 created a low-level signal of positively-tilted troughing over the eastern Mediterranean and
324 ridging poleward over northwestern Europe reflecting the orientation of upper-level troughs and
325 ridges in the wind and TSI fields in Figures 4-6 accompanying the anticyclonic RWB (e.g.,
326 Figures 7c, 8c, 9c). Following this initial break, these low-level features will be in place as the
327 second break develops. The features in place with the first break allow favorable conditions for
328 northeasterly-easterly flow along the northern Mediterranean coast of Africa particularly Libya,
329 Tunisia, and Morocco. Specifically, the low-level mass and momentum fields resulting from the
330 first break drift slowly eastward over the Mediterranean into the Middle East and eventually
331 become quasi-stationary in the absence of progressive upstream wave propagation consistent
332 with another major RWB. There, they remain anchored in place and serve to support an
333 upstream-directed low-level pressure gradient and flow directed towards the North African
334 Mediterranean and Atlantic Coastal regions. This serves to block downstream propagation of
335 pressure systems as a lateral boundary condition for the second breaking process (RWB #2) thus
336 facilitating a turning of the upstream flow towards Iberia over northwest Africa. This focuses the
337 development of moist convection and upper-level trough thinning over the northwestern part of
338 Africa allowing transport of dust polewards rather than eastwards.

339 The literature on RWB, most notably Abatzoglou and Magnusdottir (2006) as well as
340 Strong and Magnusdottir (2008) not only specifies the importance of jet separation in RWB but
341 of such separation in the wave resonance process where energy in the first break is reflected
342 poleward and amplifies the second break. Separation in the jets facilitates poleward energy
343 reflection as opposed to progressive downstream propagation of Rossby waves. This is typically
344 responsible for a massive positive tilt and arching extension of the mass and momentum
345 poleward and downstream with the second break. We see this process occur two-three days after
346 the first break sequence, ~three-five days out in Figures 4-6. As the positively-tilted trough
347 propagates downstream over central and eastern Europe as well as the Mediterranean, a new
348 break begins to form upstream from the anticyclonic IPV on 330K left over from the first break.
349 Consistent with the literature, this second break contains a geometry in the wind and mass fields
350 indicative of even greater positive (anticyclonic) tilt and equatorward as well as poleward
351 penetration of IPV and its meridional reversal as can be seen in Figures 4-6. The equatorward
352 penetration of positive IPV and poleward penetration of negative IPV is even more pronounced
353 than the first break with its motion towards northwestern Africa, i.e., the western Algerian and
354 Moroccan Coasts. This second break is every bit as baroclinic as the first if not more so, with the
355 advection of very low TSI values south-southwestwards and the establishment of a broad scale
356 environment for potential instability over northwest Africa including the region on the leeside of
357 both the Atlas and Hoggar Mountain Ranges in Algeria. In two of the three case studies, i.e., O08
358 and F16, cutoff vortices result over northwestern Africa in proximity to the Atlas Mountains as a
359 result of this RWB. In S07 an offshore preexisting upstream vortex (labeled as "3" in Figure 4) is
360 fortified by the break downstream over the eastern Mediterranean as energy builds upstream over
361 the eastern Atlantic and that preexisting vortex eventually propagates towards northwest Africa.
362 Figures 4-6 show the sequence of 330K IPV, winds, and TSI for both breaking processes and
363 their general similarity for all case studies.

364

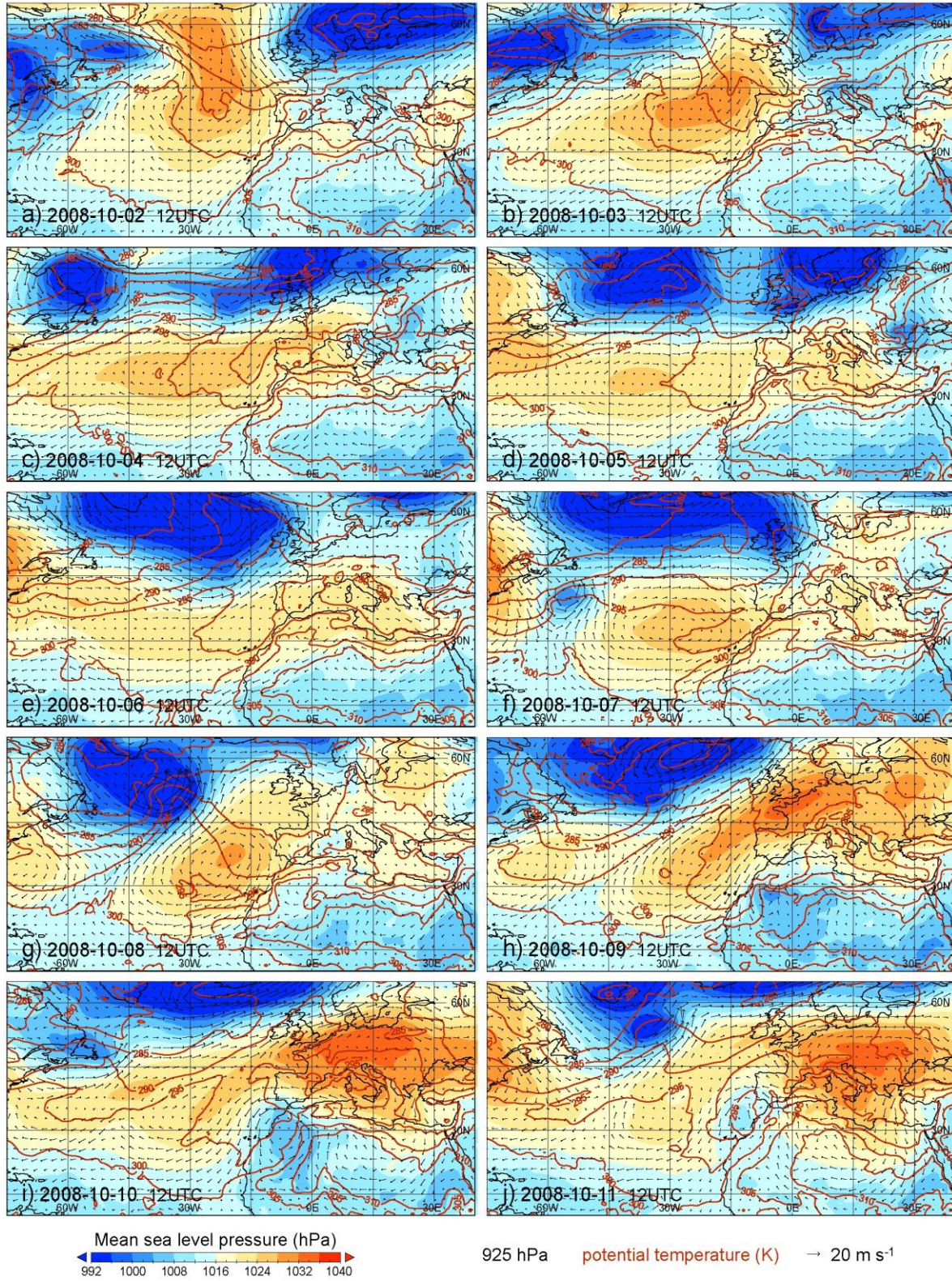


365

366

367

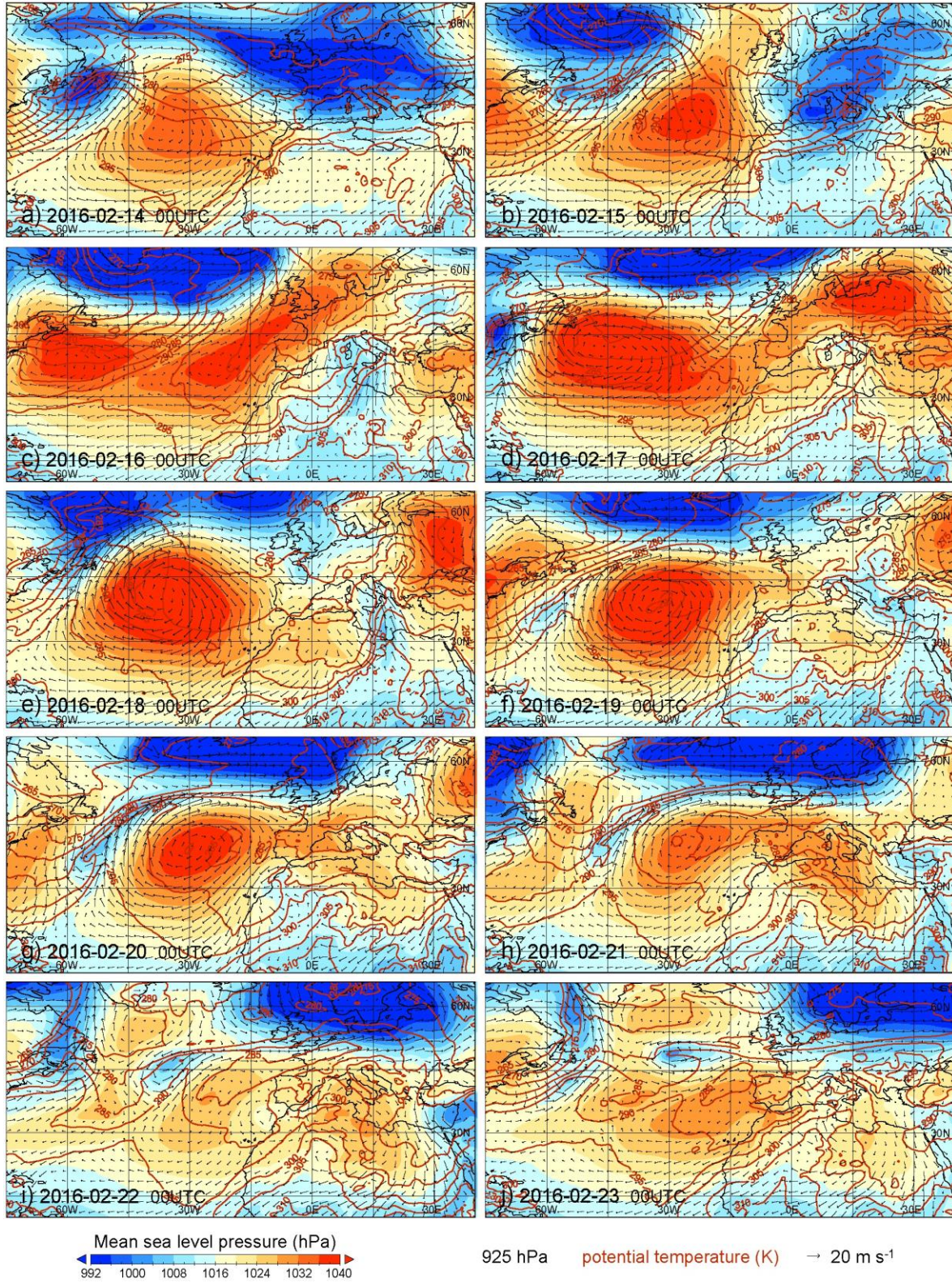
Figure 7. Mean sea level pressure (shaded), 925 hPa wind vectors and potential temperature (read contours) at the same time instants in September 2007 as in Figure 4.



368

369

Figure 8. As in Figure 7 but for October 2008 at the same time instants as in Figure 5.



370

371 **Figure 9.** As in Figure 7 but for February 2016 at the same time instants as in Figure 6.

372

373 However, substantial differences are evident among the three case studies in the location
374 and geometry of key upper- and low-level features following the second break and one-three
375 days prior to haboob and dust storm formation in Figures 4-9. In the S07 case, the wave breaking
376 is the farthest poleward and downstream over the northeastern Mediterranean yet it influences
377 the northwestern coast of Africa including the Atlas and Hoggar Mountains. In this case the
378 second break amplifies an offshore vortex west of Portugal that eventually catches up to and
379 becomes entrained into the STJ over northwest Africa. In the O08 case an extremely strong mid-
380 upper tropospheric cutoff vortex forms near the Strait of Gibraltar and continues to amplify
381 equatorward and westwards over the Atlas Mountains. In the F16 case, a similar set of
382 adjustments occurs; however, the mid-upper tropospheric vortex initially forms poleward of
383 Portugal and propagates directly equatorwards down the Atlantic Coast further strengthening
384 over the Atlas. In all three cases, however, these quasi-geostrophic RWBs set up semi-
385 geostrophic jet streak secondary circulations as the periods of wind gust front formation and
386 subsequent dust ablation occur. These circulations in conjunction with terrain-modified
387 circulations organize the potential instability and lift for the haboob-generating dust storm
388 events.

389 In spite of the differences in the three cases, including the offshore vortex in S07 and the
390 varied subsynoptic jet streak adjustments in all three, there is remarkable similarity in the double
391 RWB mechanisms. The most important similarities include: 1) the first break has a significant
392 downstream dispersive component, 2) the second break is more critical as it is meridionally
393 amplified in the trough thinning process and 3) cold air aloft acts as a unifying signal, not only
394 for the breaking process but for mesoscale adjustments within the jet streaks. Conceptual
395 depictions of the upper- and lower-level features in place are shown in Figures 16 and 17 in the
396 Summary and conclusions section.

397 Although not the focus of this work, we note that the double Rossby Wave Break process
398 in the Polar Jet implies the large scale forcing of strong cold advection over North Africa that
399 modulates (among others) the intensity and location of the North African High. Cuevas et al
400 (2017) have shown statistically that the North African Dipole Intensity (NAFDI) index and
401 derived metrics change at the intra-seasonal scale driven by the Rossby waves.

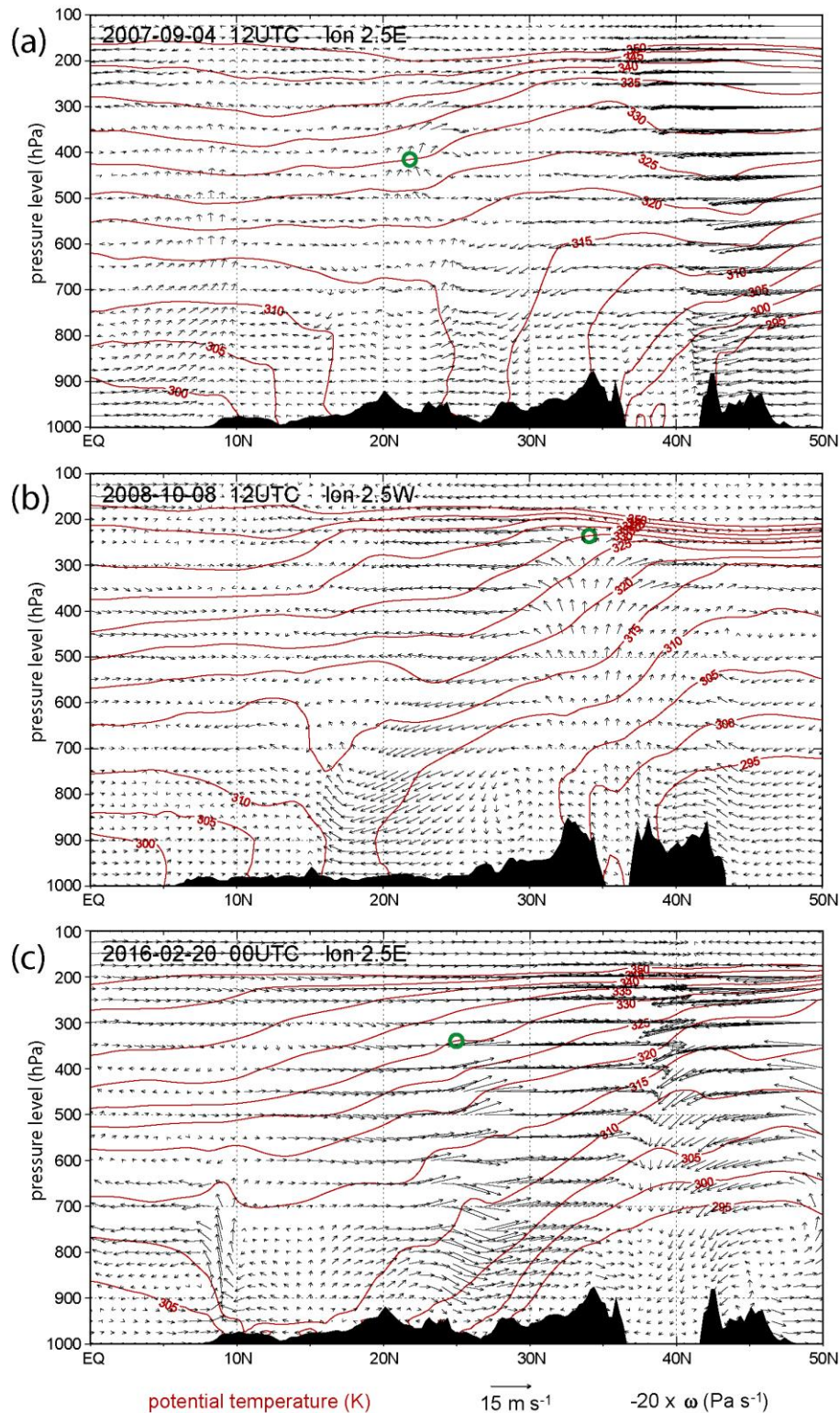
402 4.2 Jet Secondary Circulations, Moist Convective Environments, and Mountain Waves

403 The RWBs act as space-time boundary conditions and establish complex jet streak
404 adjustments at semi-geostrophic motions scales, i.e., contracting 2500-5000 km Rossby wave
405 forcing down to ~1000 km or smaller scale secondary circulations in the PJ and STJ. As the
406 second break occurs, jets intensify and produce circulations with stronger accelerating flow than
407 the larger RWBs can produce. Cold fronts strengthen and make anomalous penetrations deep
408 into Africa. The first RWB blocks the rapid downstream propagation of the STJ and PJ. Also, the
409 STJ is strengthened by the first RWB as its cold air is advected into North Africa from
410 northwestern Europe. Furthermore, the massive vortices formed aloft (O08 and F16) or enhanced
411 (S07) by the second baroclinic RWB contain newly formed southerly momentum and these new
412 PJ streaks are in place and available to interact with the streaks in the STJ enhanced by the
413 equatorward advection of cold air. The hot air over the Algerian and neighboring Saharan deserts
414 are also fortifying the streaks aloft by intensifying the TSI gradients on theta surfaces on the
415 anticyclonic side of the jets. Hence, prior to a day or two of the developing dust storms, the
416 entrance region of the STJ is propagating poleward and downstream over eastern Algeria and

417 neighboring countries and the exit region of the PJ is approaching the STJ entrance region over
418 primarily Algeria and are both now positioned such that the semi-geostrophic secondary
419 circulations can mutually interact. This interaction favors deep ascent as the PJ and STJ lift air at
420 different vertical levels which realizes the potential instability and results in moist convection in
421 the S07 and the O08 cases; in the F16 case, the jet streaks-induced deep ascent aids in the
422 destabilization process where surface heating is occurring as the air is adiabatically cooling
423 above the surface sensible heating in the southern slope of the Saharan Atlas. Since this occurs
424 over northwest Africa in proximity to the Saharan heat low, the mass perturbations caused by
425 this heat low and differential heating along the slopes of the mountains also strengthens the jet
426 circulations aloft. This interaction location between the STJ and PJ is also in proximity to hot air
427 over the Algerian deserts east of the Atlas, cool offshore maritime Atlantic air west of Morocco,
428 and relatively warm and moist air over the Mediterranean forced westwards by the mass and
429 momentum fields remaining from the first break. In addition, very warm and moist air from the
430 Intertropical Convergence Zone (ITCZ) equatorwards of Algeria over Mali whose motion
431 westwards and poleward is enhanced by the Tropical Easterly Jet (TEJ) in S07 as well as the
432 anticyclonic gyre as the STJ strengthens and rotates across northeastern Africa in O08 and F16.
433 These multi-scale processes produce differing air masses and vertically differential air mass
434 advection which are in proximity to produce moist convection in this region between the Atlas
435 and Hoggar Mountains and the Mediterranean.

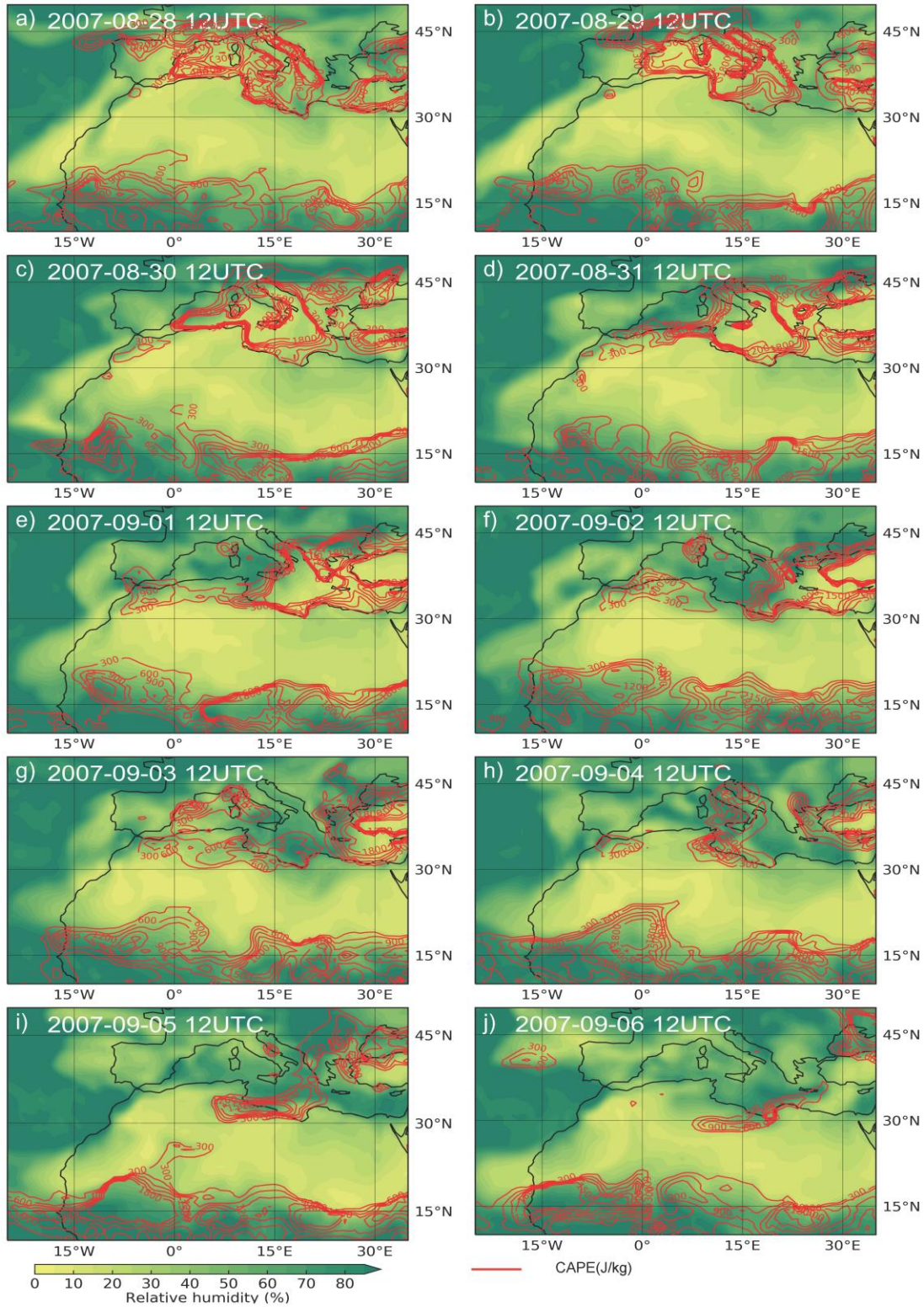
436 Figure 10 depicts vertical cross sections of winds, potential temperatures, and vertical
437 motions just prior to the images of developing convection and mountain wave activity. Figures
438 11 and 12 show distributions of convective available potential energy (CAPE) and low-level
439 relative humidity (RH) for the S07 and O08 cases. Subsequent cold convective cloud tops are
440 followed by dust ablation in MSG imagery depicted in Figures 1c-1f and 2c-2e for the S07 and
441 O08 case studies. The timing of these figures in the two cases is to show massive Mesoscale
442 Convective System (MCS) formation organizing haboobs on the windward side of the Hoggar
443 for S07 (see CAPE in Figures 11h, 11i) and leeside of the Atlas for O08 (see Figure 12h). Where
444 windward and leeside refer to the mid-upper tropospheric predominantly westerly flow in each
445 case study. Figure 13 shows the near-surface air temperature and wind vector for the F16 case
446 study at noontime. Southerly warm dry air on the foothills of the Atlas precedes the terrain-
447 induced heating perturbations (Figure 13g) accompanying dust ablation shown in MSG imagery
448 in Figures 3b-3d. The organizing mechanisms for the environment triggering convection
449 involves the development of ascent in jet secondary circulations resulting from the two RWBs
450 described above as well as extreme differential heating between the Hoggar and Atlas Mountain
451 slopes and the nearby atmosphere consistent with a mountain-plains solenoidal circulation
452 (MPS) (e.g., Tripoli & Cotton, 1989; Zhang & Koch, 2000). The MPS enhances the jet
453 circulations both: 1) directly by accompanying lifting in the warm air along the mountainside
454 exposed to solar radiation as well as planetary boundary layer (PBL) deepening and 2) indirectly
455 by enhancing the accelerations and upper-level divergence due to increasing TSI gradients on
456 that surfaces in both the newly-intensifying balanced semi-geostrophic and thermally direct STJ
457 entrance region secondary circulation and newly-intensifying PJ exit region circulations for each
458 case study.

459



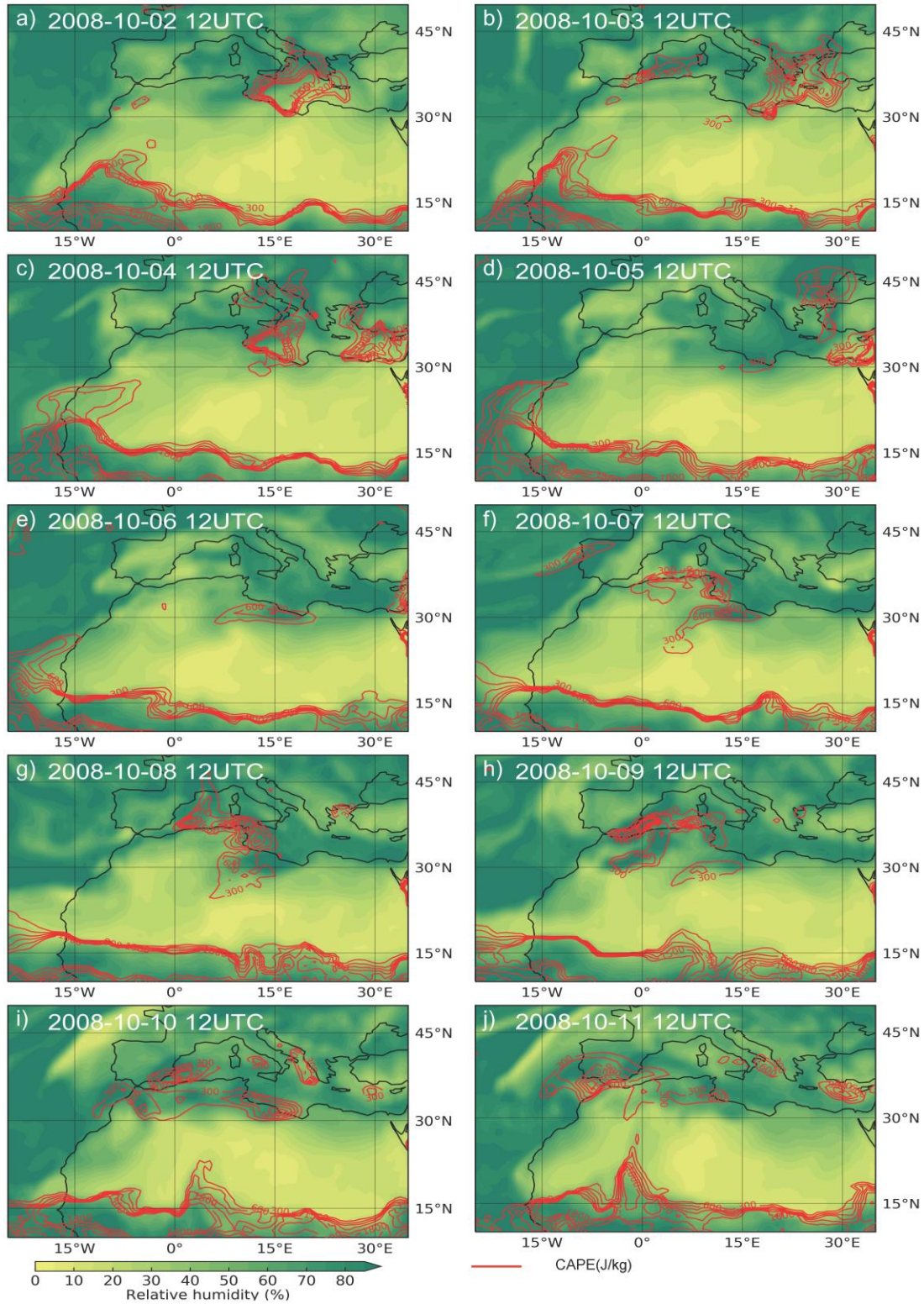
460

461 **Figure 10.** Vertical-meridional cross sections of potential temperature (line contours), and v and
 462 omega wind components (arrows) just before development of convection, for the three case
 463 studies: (a) September 2007, (b) October 2008, and (c) February 2016.



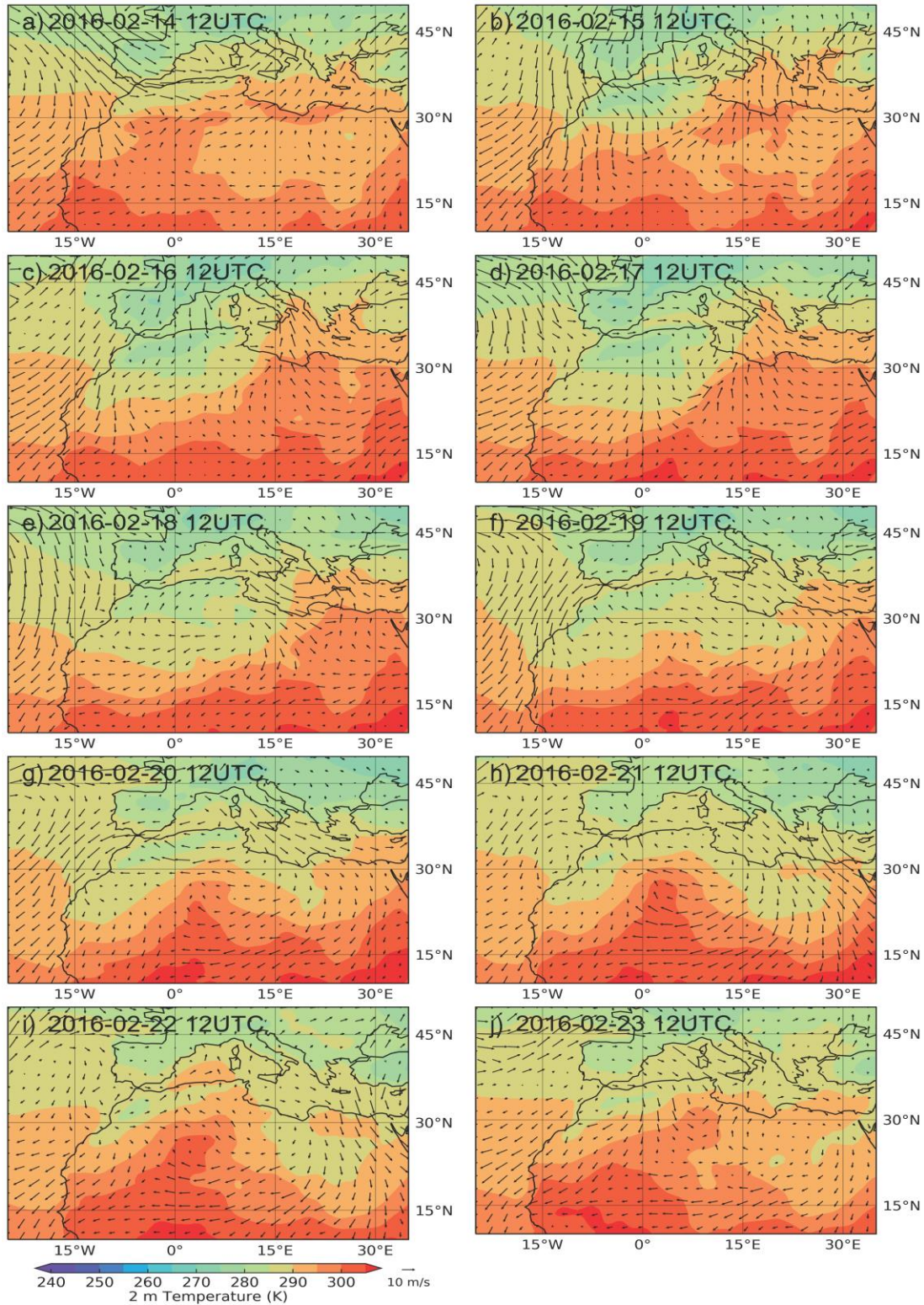
464

465 **Figure 11.** Convective available potential energy (red contours) and relative humidity (shaded)
 466 at 925 hPa at the same time instants in September 2007 as in Figure 4.



467

468 **Figure 12.** As in Figure 11 but for October 2008 at the same time instants as in Figure 5.



469

470 **Figure 13.** 2m air temperature and 10m wind at 12 UTC for the February 2016 case

471 These circulations are depicted for the three case studies along meridional vertical cross
 472 sections in Figure 10 located so as to parallel the MCS genesis processes over the mountains

473 flanking 0 degrees longitude. These vertical cross sections should be compared to Figures 7-9
474 and 11-13 which indicate general inverted low-level troughs oriented west-northwest – east-
475 southeast in all cases with even stronger low-level troughs oriented northeast-southwest in O08
476 and F16. These troughs are flanked by cutoff mid-upper tropospheric lows over the Atlas for
477 these two cases and an offshore low for S07. A broader scale Saharan heat low exists over
478 western and central Algeria. The areas of key ascent in the vertical cross sections in Figure 10
479 and corresponding jet secondary circulations in the horizontal cross sections (at the 330 K
480 surface) in Figures 4-6 are marked with a green circle. In S07 as depicted in Figure 10a, ascent
481 near 25N and 2.5E at 1200 UTC September 4 is ahead of the polar front located just equatorward
482 of 30N and strongly coupled to the anticyclonic and diverging flow in the right entrance region
483 of the STJ between 600 and 300 hPa. This is above the haboobs triggered on the western slopes
484 of the Hoggar Mountains. In O08, the key upper-level circulation is the left jet exit region ascent
485 between 30 and 35N along 2.5W at 1200 UTC on October 8 in Figure 10b. This indirect
486 circulation flanks a remarkably deep cold front aloft between 700 and 200 hPa and acts to
487 strengthen it in time. This ascent slices through the 330 K surface. This circulation supports the
488 lifting and destabilization over northwest Algeria on the northeastern slopes of the Atlas
489 Mountains. Haboob genesis here is strongly controlled by the deep cold air advection and left
490 exit region ascent accompanying the diverging flow. In F16 between 1200 UTC February 19 and
491 0000 UTC February 20 as depicted in Figure 10c, the ascent from the polar and subtropical jets’
492 left exit regions controls the regeneration of convection along the cold front over the northern
493 slopes of the Hoggar Mountains. Here the ascent shifts somewhat equatorward of the dual jets’
494 left exit regions indicating a possible unbalanced component to the upper-level diverging flow
495 extending southeastwards across the Hoggar Mountain range.

496 The low-level jets at 925 hPa in Figures 7-9 reflect the confluence of Mediterranean
497 moisture from the east, extreme Algerian heat fortified along the Hoggar and Atlas Mountain
498 slopes from the south-southwest, and cooler onshore flow from the Atlantic to the west-
499 northwest. The patterns of CAPE and RH reflect the moist air from the Mediterranean and moist
500 monsoonal air from the ITCZ undercutting hot dry Saharan air. These maxima of CAPE in the
501 preconvective environment are formed as the cold mid-upper tropospheric vortices propagate
502 equatorward and, in conjunction with ascent in the jet secondary circulations described in the
503 previous paragraph, they advect cold air equatorward and lift the air, respectively. The higher
504 CAPE air masses then organize massive moist convective systems. The favorable environment
505 for moist convection, for example, is dramatically depicted in Figure 14 where the 24-hour
506 changes in the Dar-El-Beida (DAAG) soundings are inter compared during haboob genesis on
507 the slopes of the Atlas (Figure 2). Note in Figure 14 the shift in flow to the east under hot dry
508 adiabatic conditions aloft and substantial increase in sounding CAPE between the early and late
509 time periods. This is typical of a well-mixed layer aloft being undercut by moist Mediterranean
510 air as cold air arrives in the jet exit region. This sounding is located under the equatorward
511 amplifying upper-level IPV maximum and the right entrance region of the STJ over North Africa
512 during O08 in Figures 4 and 10b as well. Mid-upper tropospheric cooling occurs in conjunction
513 with the advection of moist air under the well-mixed layer. In S07 the right entrance region of
514 the STJ is fortified by the outflow above tropical convection from the right exit region of the TEJ
515 in Figure 10a. In F16 a somewhat similar coupling of strong STJ exit region ageostrophic flow
516 and inflow from the ITCZ is evident in Figures 6 and 10c. Thus in all three cases the favorable
517 environment for deep MCS and MPS formation on the slopes of the mountains results from the
518 mid-latitude multiple RWBs as the PJ and STJ exit and entrance regions are restructured by

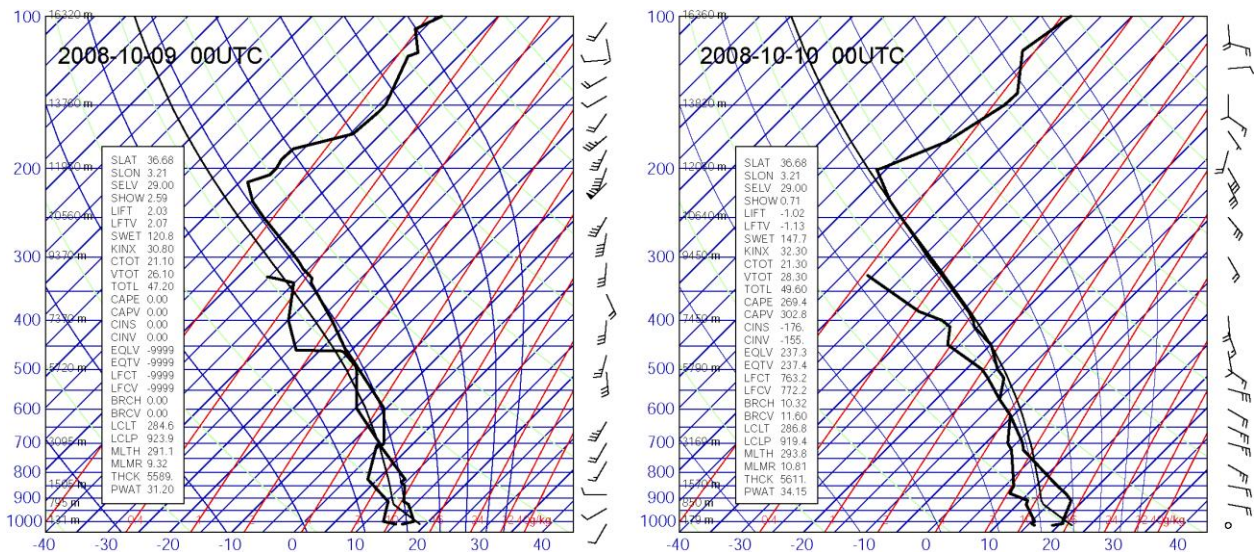
519 those wave breaking processes. As a result, moist convection develops from southwest to
520 northeast in S07 along the slopes of the Hoggar, orographic gravity wave activity builds up first
521 over the northern slopes of the Hoggar and then in the southern slopes of the Saharan Atlas in
522 F16 and very persistent multiple MCS form in O08 primarily on the downstream leeside of the
523 northern Atlas.

524 Figures 1-3 indicate that plumes of dust emanate from the convection or from the terrain-
525 induced wave activity as these features develop. In S07, convection builds northeastwards up the
526 windward slope of the Hoggar. Two distinct MCS form first near the Algerian border with Mali
527 and second northeast over western Algeria with each indicating a haboob. The haboobs generate
528 low-level outflow and the subsequent spreading of dust, first from the southwest with the first
529 MCS and then towards the northwest with the second MCS in Figure 1. These plumes merge and
530 turn northwestwards in the confluence zone between northeasterly low-level flow over
531 northeastern Algeria and southwesterly low-level flow over central Algeria in Figure 7. Aloft,
532 the lift for this convection is anchored in the region where the TEJ right exit region (Figure 4) is
533 fortified by moist convection and parcels are then turning into and accelerating into the STJ right
534 entrance region creating both speed and curvature-induced divergence in the upper troposphere
535 above a well-heated and well-mixed convective PBL over the Hoggar in Figure 10a. The arrival
536 of the mid-upper tropospheric offshore vortex in the STJ further lifts parcels rich in dust as the
537 low-level plume resulting from the merger of the two haboobs (Figure 1) approaches the Atlas
538 Mountains in the right exit region of the jet streak preceding the vortex.

539 In O08, persistent convection along the northwest African Coast extending downstream
540 across the northern Atlas Mountains organizes a haboob that propagates southwestwards towards
541 an inland propagating Atlantic onshore cool front in Figure 2. The motion of the strong dust front
542 is controlled by the Atlas guiding it southwestwards as it converges into an onshore flow of cool
543 Atlantic air equatorward of the Atlas as can be seen in the low-level flow in Figure 8. This dust
544 plume eventually turns northwards and then northwestwards (Figure 2) and is converged into a
545 cyclonic circulation in proximity to the downstream hot air in the Saharan heat low over
546 southcentral Algeria. It is subsequently joined by another plume of dust from a smaller MCS that
547 formed close to the Hoggar. These plumes converge, take on a cyclonic coma shape, and turn
548 north-northwestwards in the confluence zone setup by the merger of southeasterly hot air from
549 the Saharan heat low, northeasterly cool air from the haboob and Mediterranean, and westerly
550 cool airflow from the Atlantic. It is shown in Figure 8 that a new subsynoptic surface low forms
551 here as the dust is lifted over the Atlas. The plumes are also lifted by the strong jet entrance
552 region circulation from the STJ but more dramatically by the new PJ streak that formed ahead of
553 the mid-upper tropospheric vortex, which transports the dust over the Atlas towards the Strait of
554 Gibraltar and the Spanish Coast in Figure 10b.

555 Finally, in F16, a strong downslope wind over the northern slope of the Hoggar
556 Mountains forms under a highly accelerative region in the STJ entrance which is subsequently
557 but closely followed by very intense lifting in the exit region of a PJ streak ahead of the vortex
558 analogous to O08 in Figure 10c. However, the dust transport northwestwards in this case (Figure
559 3) is facilitated by increasing southeasterly flow up the Atlas after a break period during which
560 the PJ streak propagates over the Atlas and the Strait of Gibraltar. Remarkably strong terrain-
561 induced waves analogous to terrain-induced gravity waves form above the Atlas during this
562 transport process and likely control the lifting of the dust towards Iberia under an accelerating
563 polar jet streak entrance ahead of the upper vortex in Figure 6. These waves may also reflect the

564 strong divergence in the right exit region of this streak indicative of an unbalanced jet circulation
 565 during a period of substantial surface heating over the Saharan Atlas Mountains similar to the
 566 unbalanced circulations described in Pokharel et al. (2016).



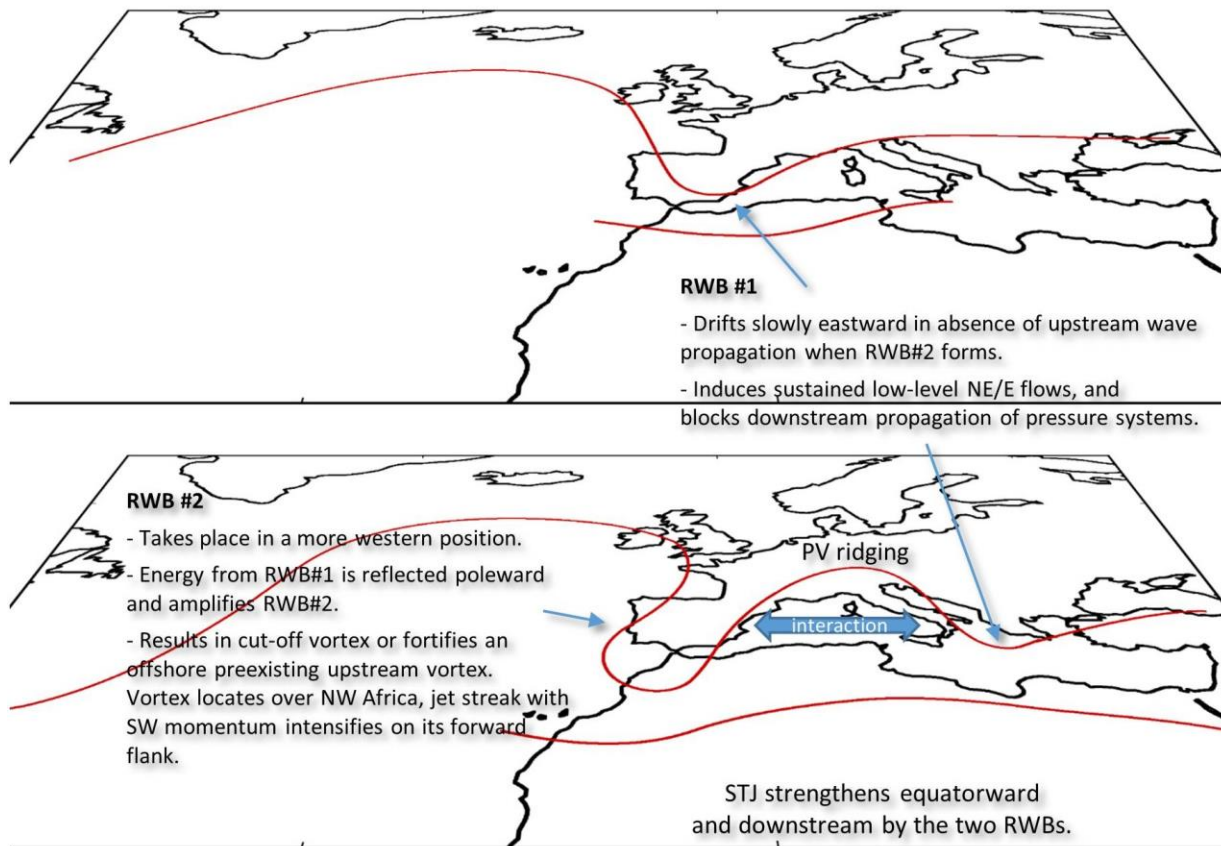
567
 568 **Figure 14.** Skew T-log p diagrams of 00UTC soundings from Dar el Beida (DAAG, 60390) in
 569 Algeria.

570 5 Summary and Conclusions

571 A sequence of multi-scale adjustments starting from continental scales and cascading
 572 down the scale of MCS are implicated in organizing multiple Saharan dust storms prior to dust
 573 transport poleward above the Iberian Peninsula. Two polar stream Rossby wave breaks represent
 574 the large scale organizing mechanisms with the first commencing nearly ten days prior to dust
 575 storm formation followed by a second three to five days later. As the two RWBs occur, both the
 576 PJ and STJ are radically restructured as is implicit in the IPV reversal process. This restructuring
 577 involves vortex intensification and equatorwards propagation during the trough thinning process
 578 over the Atlas Mountains as well as a strengthening and coupling of the STJ to circulations in the
 579 ITCZ. New PJ streaks intensify downstream from these vortices. These southwesterly streaks
 580 enhance mid-upper tropospheric cyclone formation upstream and over the Atlas and also produce
 581 low-level jets that transport hot low-level air poleward that interact with persistent cooler and
 582 moist low-level jets from the Mediterranean coastal region. MCS develop as the hot Saharan air
 583 overruns the cooler moist Mediterranean air and/or the very moist air from the ITCZ and
 584 subsequently is lifted by the jet streak secondary circulations as the cold mid-tropospheric air
 585 with each upper vortex is transported towards the equator. The potential instability that forms
 586 and is triggered by jet streak lifting generates deep and widespread MCS formation which is
 587 critical to haboob genesis that ablates surface dust. Also it is the proximity of PBL outflow from
 588 the MCS to sources of dust, deep ascent poleward of the dust generation region, and subsequent
 589 poleward transport that is critical to dust arriving over Iberia. That outflow lifts the dust and then
 590 the dust interacts with complex terrain-induced and larger scale circulations. Schematics of these
 591 complex processes as derived in this first paper from observations are depicted in Figures 15-16.

592 The double RWB mechanism, linked to nonlinear wave reflection, ultimately favors the
 593 poleward transport of dust to the Iberian Peninsula, rather than eastwards, both by the

594 amplification of the second RWB and trough thinning west or over the Atlas and by blocking
 595 zonal air flows. Perhaps the most important result of the analyses is the dominance of the polar
 596 jet, its extraordinary cold air, and its strong coupling to anticyclonic RWB. In all three case
 597 studies there is a remarkable equatorward penetration of polar air into Africa that represents an
 598 extreme cold air anomaly at progressively lower latitudes in Africa as the case studies transition
 599 from summer to autumn to winter. In fact, the signal of over-reflection is consistent with the
 600 findings of Abatzoglou & Magnusdottir (2006), but for RWBs in the polar stream over Europe in
 601 transition seasons as opposed to exclusively the subtropical tropopause over the Pacific and the
 602 Atlantic in the warm season. These authors have found non-linear reflection in a large proportion
 603 of RWBs; therefore, a large climatology of RWBs in the polar stream including the assessment
 604 of non-linear reflection and its implication in organizing Saharan dust storms is of relevance and
 605 will be conducted in the future.

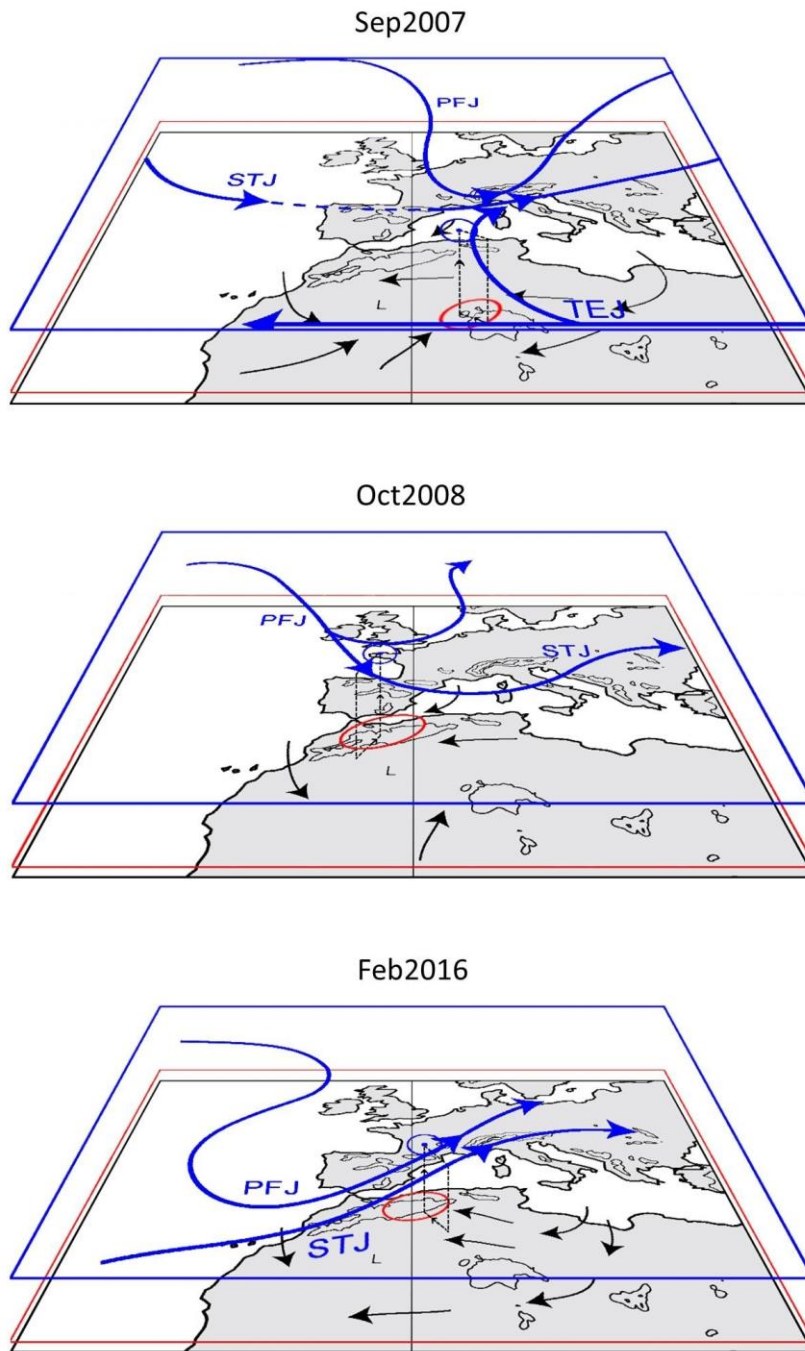


606

607 **Figure 15.** Schematic depiction of the interactions between the two polar stream Rossby wave
 608 breaks that prepare the environment for moist convection and/or mountain wave formation over
 609 North Africa, responsible for dust ablation. The western location of RWB #2 favors dust
 610 transport poleward to southwestern Europe.

611 The analysis in this first paper is derived solely from observations, as such it is lacking in
 612 detail possible in space and time from high resolution numerical model simulations. It represents
 613 a broad overview of the processes that lead to dust storms and dust transport from the Sahara to
 614 the IP in three case studies. Numerical simulations of meso- α , β , and γ -scale air trajectories and
 615 PBL circulations in proximity to complex terrain and in comparison to surface and remotely-

616 sensed atmospheric optical depth observations of dust will be analyzed in a subsequent paper,
617 Part II, to follow. This will enable a truly mesoscale analysis of the broader scale
618 observationally-derived features described in this paper.



619

620 **Figure 16.** Schematic illustration of upper-level jet circulations (blue); near-surface flows
621 (black) that undercut the stable Saharan air layer; jet streak secondary circulations (dashed black
622 lines) and areas over the Atlas and Hoggar Mountains of intense differential heating leading to
623 mountain plain solenoidal circulations (in red), both amplifying low-level convergence and
624 divergence aloft.

625 **Acknowledgments and Data**

626 This work is partially funded by the Spanish Ministerio de Economía y Competitividad
627 and EU FEDER under grant CGL2015-70741-R (FRESA Project). J.A.G.O. acknowledges the
628 Regional Government of Valencia (grant BEST/2018/091) for partial support of a research visit
629 at DRI in summer 2018, and thanks DRI and Prof. Kaplan for hosting him.

630 We thank ECMWF for making available the ERA-Interim reanalysis data
631 (<https://www.ecmwf.int/en/forecasts/datasets/reanalysis-datasets/era-interim>), EUMETSAT for
632 the SEVIRI MSG data (available at <https://eoportal.eumetsat.int/> after registration),
633 NOAA/ESRL for the provision of the HYSPLIT model, and the University of Wyoming for
634 providing access to their radiosounding database.

635 **References**

- 636 Abatzoglou, J.T., & Magnusdottir, G. (2006). Planetary wave breaking and nonlinear reflection:
637 Seasonal cycle and interannual variability. *Journal of Climate*, 19, 6139–6152.
638 <https://doi.org/10.1175/JCLI3968.1>
- 639 Adams, A.M., Prospero, J.M., & Zhang, C. (2012). CALIPSO-derived three-dimensional
640 structure of aerosol over the Atlantic basin and adjacent continents. *Journal of Climate*,
641 25, 6862–6879. <https://doi.org/10.1175/JCLI-D-11-00672.1>
- 642 Alpert, P., & Ziv, B. (1989). The Sharav cyclone - observations and some theoretical
643 considerations. *Journal of Geophysical Research*, 94(D15), 18,495–18,514.
644 <https://doi.org/10.1029/JD094iD15p18495>
- 645 Antón, M., Sorribas, M., Bennouna, Y., Vilaplana, J.M., Cachorro, V.E., Gröbner, J., Alados-
646 Arboledas, L. (2012). Effects of an extreme desert dust event on the spectral ultraviolet
647 irradiance at El Arenosillo (Spain). *Journal of Geophysical Research: Atmospheres*, 117,
648 D03205. <https://doi.org/10.1029/2011JD016645>
- 649 Barkan, J., Alpert, P., Kutiel, H., & Kishcha, P. (2005). Synoptics of dust transportation days
650 from Africa toward Italy and central Europe. *Journal of Geophysical Research:*
651 *Atmospheres*, 110, D07208. <https://doi.org/10.1029/2004JD005222>
- 652 Brindley, H., Knippertz, P., Ryder, C., & Ashpole, I. (2012). A critical evaluation of the ability
653 of the Spinning Enhanced Visible and Infrared Imager (SEVIRI) thermal infrared red-
654 green-blue rendering to identify dust events: Theoretical analysis. *Journal of Geophysical*
655 *Research*, 117, D07201. <https://doi.org/10.1029/2011JD017326>
- 656 Cabello, M., Orza, J.A.G., Barrero, M.A., Gordo, E., Berasaluce, A., Cantón, L., et al. (2012).
657 Spatial and temporal variation of the impact of an extreme Saharan dust event. *Journal of*
658 *Geophysical Research*, 117, D11204. <https://doi.org/10.1029/2012JD017513>
- 659 Cazorla, A., Casquero-Vera, J.A., Román, R., Guerrero-Rascado, J.L., Toledano, C., Cachorro,
660 V.E., et al. (2017). Near-real-time processing of a ceilometer network assisted with sun-
661 photometer data: monitoring a dust outbreak over the Iberian Peninsula. *Atmospheric*
662 *Chemistry and Physics* 17, 11,861–11,876. <https://doi.org/10.5194/acp-17-11861-2017>
- 663 Cuevas, E., Gómez-Peláez, A.J., Rodríguez, S., Terradellas, E., Basart, S., García, O.M. &
664 Alonso-Pérez, S. (2017). The pulsating nature of large-scale Saharan dust transport as a
665 result of the interplays between mid-latitude Rossby waves and the North African Dipole

- 666 Intensity. *Atmospheric Environment* 167, 586-602.
667 <https://doi.org/10.1016/j.atmosenv.2017.08.059>
- 668 Dayan, U., Ziv, B., Shoob, T., & Enzel, Y. (2008). Suspended dust over southeastern
669 Mediterranean and its relation to atmospheric circulations. *International Journal of*
670 *Climatology*, 28, 915–924. <https://doi.org/10.1002/joc.1587>
- 671 Dee, D.P., et al. (2011). The ERA-Interim reanalysis: Configuration and performance of the data
672 assimilation system. *Quarterly Journal of the Royal Meteorological Society*, 137, 553–
673 597. <https://doi.org/10.1002/qj.828>
- 674 Escudero M., Castillo S., Querol X., Avila A., Alarcón M., Viana M.M., et al. (2005). Wet and
675 dry African dust episodes over Eastern Spain. *Journal of Geophysical Research*, 110,
676 D18S08. <https://doi.org/10.1029/2004JD004731>
- 677 Fiedler, S., Schepanski, K., Knippertz, P., Heinold, B., & Tegen, I. (2014). How important are
678 atmospheric depressions and mobile cyclones for emitting mineral dust aerosol in North
679 Africa? *Atmospheric Chemistry and Physics*, 14(17), 8983–9000.
680 <https://doi.org/10.5194/acp-14-8983-2014>
- 681 Fiedler, S., Kaplan, M.L., & Knippertz, P. (2015). The importance of Harmattan surges for the
682 emission of North African dust aerosol. *Geophysical Research Letters*, 42, 9495–9504.
683 <https://doi.org/10.1002/2015GL065925>
- 684 Flaounas, E., Kotroni, V., Lagouvardos, K., Kazadzis, S., Gkikas, A., & Hatzianastassiou, N.
685 (2015). Cyclone contribution to dust transport over the Mediterranean region.
686 *Atmospheric Science Letters*, 16, 473–478. <https://doi.org/10.1002/asl.584>
- 687 Francis, D., Eayrs, C., Chaboureaud, J.-P., Mote, T., & Holland, D.M. (2018). Polar Jet
688 Associated Circulation Triggered a Saharan Cyclone and Derived the Poleward Transport
689 of the African Dust Generated by the Cyclone. *Journal of Geophysical Research:*
690 *Atmospheres*, 123, 11,899–11,917. <https://doi.org/10.1029/2018JD029095>
- 691 Ganor, E., Osetinsky, I., Stupp, A., & Alpert, P. (2010). Increasing trend of African dust, over 49
692 years, in the eastern Mediterranean. *Journal of Geophysical Research*, 115, D07201.
693 <https://doi.org/10.1029/2009JD012500>
- 694 Gkikas, A., Hatzianastassiou, N., & Mihalopoulos, N. (2009). Aerosol events in the broader
695 Mediterranean basin based on 7-year (2000–2007) MODIS C005 data. *Annales*
696 *Geophysicae*, 27, 3509–3522. <https://doi.org/10.5194/angeo-27-3509-2009>
- 697 Gkikas, A., Hatzianastassiou, N., Mihalopoulos, N., Katsoulis, V., Kazadzis, S., Pey, J., et al.
698 (2013). The regime of intense desert dust episodes in the Mediterranean based on
699 contemporary satellite observations and ground measurements. *Atmospheric Chemistry*
700 *and Physics*, 13, 12,135–12,154. <https://doi.org/10.5194/acp-13-12135-2013>
- 701 Gläser, G., Wernli, H., Kerkweg, A., & Teubler, F. (2015). The transatlantic dust transport from
702 North Africa to the Americas—Its characteristics and source regions. *Journal of*
703 *Geophysical Research: Atmospheres*, 120, 11,231–11,252.
704 <https://doi.org/10.1002/2015JD023792>
- 705 Guerrero-Rascado, J.L., Olmo, F.J., Avilés-Rodríguez, I., Navas-Guzmán, F., Pérez Ramírez, D.,
706 Lyamani, H., & Alados Arboledas, L. (2009). Extreme Saharan dust event over the

707 southern Iberian Peninsula in september 2007: active and passive remote sensing from
708 surface and satellite. *Atmospheric Chemistry and Physics*, 9, 8453–8469.
709 <https://doi.org/10.5194/acp-9-8453-2009>

710 Israelevich, P.L., Levin, Z., Joseph, J.H., & Ganor, E. (2002). Desert aerosol transport in the
711 Mediterranean region as inferred from the TOMS aerosol index. *Journal of Geophysical*
712 *Research*, 107(D21), 4572. <https://doi.org/10.1029/2001JD002011>

713 Israelevich, P., Ganor, E., Alpert, P., Kishcha, P., & Stupp, A. (2012). Predominant transport
714 paths of Saharan dust over the Mediterranean Sea to Europe. *Journal of Geophysical*
715 *Research*, 117, D02205. <https://doi.org/10.1029/2011JD016482>

716 Knippertz, P., & Todd, M.C. (2012). Mineral dust aerosols over the Sahara: meteorological
717 controls on emission and transport and implications for modeling. *Reviews of*
718 *Geophysics*, 50, RG1007. <https://doi.org/10.1029/2011RG000362>

719 Lensky, I.M. and Rosenfeld, D. (2008). Clouds-Aerosols-Precipitation Satellite Analysis Tool
720 (CAPSAT). *Atmospheric Chemistry and Physics*, 8, 6739–6753.
721 <https://doi.org/10.5194/acp-8-6739-2008>

722 Marinou, E., Amiridis, V., Biniotoglou, I., Tsikerdekis, A., Solomos, S., Proestakis, E., et al.
723 (2017). Three-dimensional evolution of Saharan dust transport towards Europe based on
724 a 9-year EARLINET-optimized CALIPSO dataset. *Atmospheric Chemistry and Physics*,
725 17, 5893–5919. <https://doi.org/10.5194/acp-17-5893-2017>

726 Moulin, C., Lambert, C.E., Dayan, U., Masson, V., Ramonet, M., Bousquet, P., et al. (1998).
727 Satellite climatology of African dust transport in the Mediterranean atmosphere. *Journal*
728 *of Geophysical Research*, 103(D11), 13,137–13,144. <https://doi.org/10.1029/98JD00171>

729 Pey, J., Querol, X., Alastuey, A., Forastiere, F., & Stafoggia, M. (2013). African dust outbreaks
730 over the Mediterranean Basin during 2001–2011: PM10 concentrations, phenomenology
731 and trends, and its relation with synoptic and mesoscale meteorology. *Atmospheric*
732 *Chemistry and Physics*, 13, 1395–1410. <https://doi.org/10.5194/acp-13-1395-2013>

733 Pokharel, A.K., Kaplan, M.L., & Fiedler, S. (2017). Subtropical Dust Storms and Downslope
734 Wind Events. *Journal of Geophysical Research: Atmospheres*, 122, 10,191–10,205.
735 <https://doi.org/10.1002/2017JD026942>

736 Postel, G.A., & Hitchman, M.H. (1999). A climatology of Rossby wave breaking along the
737 subtropical tropopause. *Journal of Atmospheric Science*, 56, 359–373.
738 [https://doi.org/10.1175/1520-0469\(1999\)056<0359:ACORWB>2.0.CO;2](https://doi.org/10.1175/1520-0469(1999)056<0359:ACORWB>2.0.CO;2)

739 Prospero, J.M. (1999). Long-term measurements of the transport of African mineral dust to the
740 southeastern United States: Implications for regional air quality. *Journal of Geophysical*
741 *Research*, 104, 15,917–15,928. <https://doi.org/10.1029/1999JD900072>

742 Querol, X., Pey, J., Pandolfi, M., Alastuey, A., Cusack, M., Pérez, N., et al. (2009). African dust
743 contributions to mean ambient PM10 mass-levels across the Mediterranean Basin.
744 *Atmospheric Environment*, 43, 4266–4277.
745 <https://doi.org/10.1016/j.atmosenv.2009.06.013>

746 Rodríguez, S., Querol, X., Alastuey, A., Kallos, G., & Kakaliagou, O. (2001). Saharan dust
747 contributions to PM10 and TSP levels in Southern and Eastern Spain. *Atmospheric*
748 *Environment*, 35, 2433–2447. [https://doi.org/10.1016/S1352-2310\(00\)00496-9](https://doi.org/10.1016/S1352-2310(00)00496-9)

749 Salvador, P., Alonso-Pérez, S., Pey, J., Artíñano, B., de Bustos, J.J., Alastuey, A., & Querol, X.
750 (2014). African dust outbreaks over the western Mediterranean Basin: 11-year
751 characterization of atmospheric circulation patterns and dust source areas. *Atmospheric*
752 *Chemistry and Physics*, 14, 6759–6775. <https://doi.org/10.5194/acp-14-6759-2014>

753 Schepanski, K., Tegen, I., Laurent, B., Heinold, B., & Macke, A. (2007). A new Saharan dust
754 source activation frequency map derived from MSG-SEVIRI IR channels. *Geophysical*
755 *Research Letters*, 34, L18803. <https://doi.org/10.1029/2007GL030168>

756 Schepanski, K., Tegen, I., Todd, M.C., Heinold, B., Bönisch, G., Laurent, B., et al. (2009).
757 Meteorological processes forcing Saharan dust emission inferred from MSG-SEVIRI
758 observations of sub-daily dust source activation. *Journal of Geophysical Research*, 114,
759 D10201. <https://doi.org/10.1029/2008JD010325>

760 Schepanski, K., Heinold, B., & Tegen, I. (2017). Harmattan, Saharan heat low, and West African
761 monsoon circulation: modulations on the Saharan dust outflow towards the North
762 Atlantic, *Atmospheric Chemistry and Physics* 17, 10223-10243.
763 <https://doi.org/10.5194/acp-17-10223-2017>

764 Sorribas, M., Adame, J.A., Andrews, E., Yela, M. (2017). An anomalous African dust event and
765 its impact on aerosol radiative forcing on the Southwest Atlantic coast of Europe in
766 February 2016. *Science of the Total Environment*, 583, 269–279.
767 <https://doi.org/10.1016/j.scitotenv.2017.01.064>

768 Strong, C., & Magnusdottir, G. (2008). Tropospheric Rossby wave breaking and the NAO/NAM.
769 *Journal of Atmospheric Sciences*, 65, 2861–2876.
770 <https://doi.org/10.1175/2008JAS2632.1>

771 Titos, G., Ealo, M., Pandolfi, M., Pérez, N., Sola, Y., Sicard, M., et al. (2017). Spatiotemporal
772 evolution of a severe winter dust event in the western Mediterranean: Aerosol optical and
773 physical properties. *Journal of Geophysical Research: Atmospheres*, 122, 4052–4069.
774 <https://doi.org/10.1002/2016JD026252>

775 Tripoli, G.J., & Cotton, W.R. (1989). A numerical study of an observed orogenic mesoscale
776 convective system. Part II: Analysis of governing dynamics. *Monthly Weather Review*,
777 117, 305–328. [https://doi.org/10.1175/1520-0493\(1989\)117<0305:NSOAOO>2.0.CO;2](https://doi.org/10.1175/1520-0493(1989)117<0305:NSOAOO>2.0.CO;2)

778 Varga, G., Újvári, G., & Kovács, J. (2014). Spatiotemporal patterns of Saharan dust outbreaks
779 in the Mediterranean Basin. *Aeolian Research*, 15, 151–160.
780 <https://doi.org/10.1016/j.aeolia.2014.06.005>

781 Zhang, F., & Koch, S.E. (2000). Numerical simulations of a gravity wave event over CCOPE.
782 Part II: Waves generated by an orographic density current. *Monthly Weather Review*,
783 128, 2777–2796. [https://doi.org/10.1175/1520-0493\(2000\)128<2777:NSOAGW>2.0.CO;2](https://doi.org/10.1175/1520-0493(2000)128<2777:NSOAGW>2.0.CO;2)

784
785